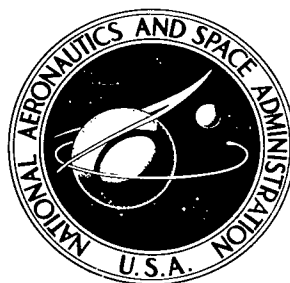


NASA TECHNICAL NOTE



NASA TN D-4591

C. 1



NASA TN D-4591

LOAN COPY: RETURN TO  
AFWL (WLIL-2)  
KIRTLAND AFB, N MEX

# FLUCTUATING PRESSURES ON THE AFTERBODIES OF FIVE BLUNT ATMOSPHERE ENTRY VEHICLES

*by Robert C. Robinson, Bruno J. Gambucci,  
and Robert E. George*

*Ames Research Center  
Moffett Field, Calif.*



NATIONAL AERONAUTICS AND SPACE ADMINISTRATION • WASHINGTON, D. C. • MAY 1968



FLUCTUATING PRESSURES ON THE AFTERBODIES OF FIVE  
BLUNT ATMOSPHERE ENTRY VEHICLES

By Robert C. Robinson, Bruno J. Gambucci,  
and Robert E. George

Ames Research Center  
Moffett Field, Calif.

NATIONAL AERONAUTICS AND SPACE ADMINISTRATION

---

For sale by the Clearinghouse for Federal Scientific and Technical Information  
Springfield, Virginia 22151 - CFSTI price \$3.00

FLUCTUATING PRESSURES ON THE AFTERBODIES OF FIVE  
BLUNT ATMOSPHERE ENTRY VEHICLES

By Robert C. Robinson, Bruno J. Gambucci,  
and Robert E. George

Ames Research Center

SUMMARY

Pressure fluctuations were measured on the afterbodies of entry-vehicle configurations at angles of attack from  $-14^\circ$  to  $+14^\circ$  and Mach numbers from 0.60 to 3.50. The Reynolds number range was  $2.0 \times 10^6$  to  $6.5 \times 10^6$  based on model diameter.

The models were typical of configurations which have been considered as entry vehicles for the Mars atmosphere. Forebody fineness ratios were  $1/3$  and  $1/8$  and the afterbodies were conical with half angles of  $30^\circ$ ,  $60^\circ$ , and  $80^\circ$ .

The pressure fluctuations measured at subsonic Mach numbers were of low reduced frequency (below 0.30) and were highly correlated. At supersonic Mach numbers the bandwidth of the fluctuations increased and the degree of correlation decreased with increasing Mach number.

INTRODUCTION

Vehicles which enter the Mars atmosphere at a velocity of 3 to 6 km/sec, and are required to slow down to a low speed for landing or experiment purposes, must be made very light in relation to their frontal area (see, e.g., refs. 1 and 2). This places a premium on the minimization of structural weight. An important fraction of that weight can occur in the afterbody fairing, which is subject to relatively low steady-pressure loading, but may be subject to oscillating loads due to unsteadiness of the flow off the body base. To evaluate the effect of that loading on the structure it is necessary to know the spectral density and spatial correlation as well as the level of the fluctuating pressures. Such information has not been available for the afterbodies of the very blunt configurations being considered for Mars entry. To provide such data a series of wind-tunnel tests was made in which the pressure fluctuations were measured on the afterbodies of five related entry-vehicle configurations at subsonic and supersonic Mach numbers.

## SYMBOLS

A	frontal area
B	bandwidth, Hz
$C_D$	drag coefficient
$C_p$	$\frac{p - p_\infty}{q_\infty}$
$\Delta C_{p_{rms}}$	$\frac{\Delta p_{rms}}{q_\infty}$
D	model diameter, cm
FPL	fluctuating pressure level, $\Delta p_{rms}$ converted to dB (re reference pressure of $2 \times 10^{-5} \text{ N/m}^2$ )
h	altitude, km
k	Strouhal number, $\frac{\omega D}{V_\infty}$
M	Mach number; or mass, kg
p	local static pressure, $\frac{N}{m^2}$
$p_\infty$	free-stream static pressure, $\frac{N}{m^2}$
$p_i(t)$	time history of pressure fluctuation at a P.T., $i = 1, 2, 3, 4, 5$
P.T.	pressure transducer
$q_\infty$	free-stream dynamic pressure, $\frac{N}{m^2}$
R	Reynolds number based on free-stream properties and model diameter
t	time, sec
T	sample length, sec
$V_\infty$	free-stream velocity, $\frac{m}{s}$
$\alpha$	angle of attack, deg
$\gamma_i$	initial entry angle, deg
$\delta$	afterbody angle, deg
$\xi$	distance along the afterbody, cm

$\rho$  correlation coefficient,  $\frac{R_{ij}(\tau)}{\sqrt{R_i(\tau)R_j(\tau)}}$  at  $\tau = 0$

where

$$R_i(\tau) = \frac{1}{T} \int_0^T p_i(t)p_i(t + \tau)dt$$

and

$$R_{ij}(\tau) = \frac{1}{T} \int_0^T p_i(t)p_j(t + \tau)dt \quad i, j = 1, 2, 3, 4, 5$$

$\tau$  delay time, sec

$\omega$  angular frequency,  $\frac{\text{rad}}{\text{s}}$

## APPARATUS AND PROCEDURE

### Models

Figure 1 shows the five models tested. One nose configuration was a spherically blunted right circular cone and the other a spherical segment. The afterbodies were frustums of right circular cones with half angles of  $30^\circ$ ,  $60^\circ$ , and  $80^\circ$ . A short cylindrical section formed the transition from the nose to the afterbody section. The models were mounted on a sting 7.5 cm in diameter and 100 cm long which, in turn, was mounted in an adapter 10 cm in diameter and 75 cm long. Figure 2 is a photograph of model B mounted in the 11-Foot Transonic Wind Tunnel.

### Instrumentation

Flush-mounted pressure transducers 1/8 inch in diameter were used to measure the fluctuating pressures. A semiconductor strain element, which responds to deflection of the transducer diaphragm, is connected in a bridge circuit. The other legs of the bridge are an inactive temperature compensating element within the transducer and two matching resistances in a temperature compensating module located at the instrumentation console. Each transducer was referenced to an adjacent static pressure orifice through small tubing of sufficient length to damp out fluctuations in the reference pressure. Figure 3 shows the location of the pressure transducers in the three afterbodies. In figure 4, the five transducers can be seen mounted in the afterbody of model B.

The static calibration and frequency response of a typical transducer are shown in figure 5. Static calibrations of the transducers were linear and highly repeatable beyond the  $7.0 \times 10^3 \text{ N/m}^2$  (1.0 psi) required in these tests.

Dynamic calibrations against a standard microphone in a progressive wave tube showed that the frequency responses of the pressure transducers were flat within  $\pm 1/2$  dB from 60 to 5,000 Hz.

The principal components of the instrumentation used in recording the fluctuating pressure data are shown in the block diagram of figure 6. After passing through the temperature compensating module, the fluctuating signal from the transducer is amplified by a differential amplifier. The output of the amplifier is filtered to remove any D.C. bias and is then recorded on magnetic tape. The recorded data were analyzed on analog equipment to obtain the integrated root mean square of the pressure fluctuations over the full length of each record, the power spectral density, and the spatial correlation along the surface of the models. The frequency response of the complete recording circuit is shown by the dashed curve in figure 7. The solid curve shows the combined frequency response for the recording circuit and the analog computer used for the root-mean-square measurements. Before and after each test the static calibration of each transducer was checked at the output of the differential amplifier, and a precise 1 V rms sine wave was recorded on each tape track to provide a calibrated reference for the data analysis. Before each data point was recorded, the output of the transducers was monitored on an oscilloscope and a true rms meter so that the level could be adjusted by calibrated gain changes to match the dynamic range of the tape recorder. All of the data samples were 21 seconds long.

#### Tests

The tests were conducted in the Ames 11- by 11-foot (3.35x3.35 m) transonic, 9- by 7-foot (2.74x2.13 m) supersonic, and 8- by 7-foot (2.44x2.13 m) supersonic wind tunnels. The Mach number was varied from 0.60 to 1.38 in the transonic wind tunnel and from 1.55 to 3.50 in the supersonic wind tunnels. The model angle of attack ranged from  $+14^\circ$  to  $-14^\circ$  except in the 8- by 7-foot wind tunnel where  $-13^\circ$  was the maximum negative angle obtainable. Mach number and Reynolds number conditions of the tests are shown in figure 8.

### RESULTS AND DISCUSSION

#### Static Pressures

The variation of the static pressure coefficient with Mach number at three points on the afterbodies of models A and B is shown in figure 9. These data are typical of all the static pressure data measured in the tests. As would be expected for separated flow, the effect of  $\alpha$ ,  $\delta$ , and  $\xi$  is relatively small. Above  $M = 1.20$ ,  $C_p$  varies approximately as  $1/m^2$  showing the afterbody static pressure to be nearly a constant percentage of the free-stream static pressure.

## Fluctuating Pressures

The root mean square of the fluctuating pressure level obtained from the analog computer was reduced to a fluctuating pressure coefficient,  $\Delta C_{p_{rms}}$ , which is plotted against angle of attack in figures 10 to 14 for all of the configurations and test conditions. Note that each page contains the data for only one transducer which is located as shown on the included sketch. The effect of angle of attack on  $\Delta C_{p_{rms}}$  was small and was practically identical for all of the transducers on a given configuration at a given Mach number. There was no significant change in  $\Delta C_{p_{rms}}$  due to the changes in configuration, and in most cases, the results were identical for the high and low Reynolds numbers.

The effect of Mach number on the pressure fluctuations is shown in figure 15 for  $\alpha = 4^\circ$  (the maximum  $\Delta C_{p_{rms}}$  generally occurred at that angle). Subsonically the pressure fluctuations are approximately a constant percentage of the dynamic pressure. Between  $M = 1.00$  and  $M = 2.00$  there is a transition region in which  $\Delta C_{p_{rms}}$  drops rapidly with increasing Mach number while for  $M > 2.00$ ,  $\Delta C_{p_{rms}}$  is again nearly constant.

Expressed as a percentage of free-stream static pressure the fluctuations are more nearly constant over this Mach number range. There is a maximum at about  $M = 1.00$  followed by a transition region to  $M = 2.00$ . Above  $M = 2.00$ ,  $\Delta p_{rms}/p_\infty$  rises slowly again and at  $M = 3.5$  it is about the same level as at  $M = 1.00$ .

The random nature of the pressure fluctuations requires that they be analyzed statistically for use in calculating the response of vehicle structures. Analysis of random data is treated extensively in reference 3 and the response of structures to random loading is discussed in references 4, 5, and 6. Representative samples of the present data were analyzed for power spectral density and for cross correlation between transducers. The spectra for models A and B at  $\alpha = 4^\circ$  shown in figures 16 and 17 have a shape characteristic of bandwidth-limited random noise. The frequency for 1/2 power is a measure of the bandwidth of such spectra. Approximate values of this frequency are shown in the following table.

FREQUENCY AT 1/2 POWER

M	0.6	1.00	1.38	3.00
$\delta = 80^\circ$	30 Hz	40 Hz	160 Hz	250 Hz
	$k = 0.289$	$k = 0.241$	$k = 0.744$	$k = 0.742$
$\delta = 30^\circ$	20 Hz	15 Hz	100 Hz	190 Hz
	$k = 0.194$	$k = 0.091$	$k = 0.466$	$k = 0.563$

It is evident that only very low structural frequencies would be excited subsonically while a broader range of structural modes would be affected at supersonic Mach numbers.

The concentration of energy at very low frequencies for  $M = 0.60$  and  $1.00$  indicates that the  $\Delta C_{p_{rms}}$  data for the subsonic Mach numbers are probably somewhat below the true values due to the low-frequency attenuation in the recording and analysis instrumentation. Comparison of the root-mean-square voltages from the analog computer with those read during the test from a true rms meter showed that the additional loss in the analog computer was between 5 and 10 percent for the Mach numbers below  $1.00$ .

From the power spectra an estimate can be made of the statistical accuracy of the data samples recorded in the tests. Using the narrowest bandwidth of  $15$  Hz, from the table, and the sample length of  $20$  seconds gives a BT product of  $300$ . The corresponding normalized standard error (as defined in ref. 3, pp. 182-210) for mean square values is  $0.06$ .

Both autocorrelation and cross-correlation functions were computed for several test conditions using an analog correlation computer. In general, the cross-correlation functions were a maximum at  $\tau = 0$  and decayed exponentially with increasing  $\tau$  at about the same rate as the autocorrelation functions, indicating that the cross spectra are of essentially the same shape as the spectra for the individual transducers. Therefore, the correlation coefficient, a measure of the spatial correlation, and the measured  $\Delta C_{p_{rms}}$  should give a good estimate of the overall random loading on the afterbodies. The variation of the correlation-function coefficient  $\rho$  with distance along the afterbody is shown in figures 18 and 19 for model A and in figures 20 and 21 for model B. For both configurations there is a high degree of correlation at the lower Mach numbers and angles of attack of  $0^\circ$  and  $4^\circ$ . At the larger angles of attack and at supersonic Mach numbers, the rate of decrease in  $\rho$  along the afterbodies is much greater.

To investigate the FPL that might be experienced during entry to the Mars atmosphere, the level at P.T. 3 on model B was computed for several sets of entry conditions using the values of  $\Delta C_{p_{rms}}$  shown for  $\alpha = 4^\circ$ . The two cases in figure 22 represent the extremes of FPL obtained from the calculations. In both cases, the entry was from a  $244$  km orbit at an initial velocity of  $3.65$  km/s into the VM 3 atmosphere (the characteristics of which are tabulated in ref. 7) with an  $L/D$  of  $0.25$ . The dashed portions of the FPL curves were computed from extrapolations of the data. It was assumed that  $\Delta C_{p_{rms}}$  remained constant at the value for  $M = 3.50$  for Mach numbers greater than  $3.50$ , and  $\Delta C_{p_{rms}}$  for  $M = 0.60$  was used to extend the FPL curve to lower Mach numbers.

For the case shown in figure 22(a), the maximum dynamic pressure occurred at  $M = 9.00$  and an altitude of  $84$  km. However, the FPL at  $q_{max}$  was only  $92$  dB compared to the maximum FPL of  $107$  dB which would occur at  $M = 1.00$  and  $h = 40$  km.

With a heavier vehicle, figure 22(b), a much higher maximum dynamic pressure was obtained at an altitude of 40 km and  $M = 9.00$ . This pressure resulted in a FPL of about 115 dB which was reached again when the vehicle had decelerated to the terminal Mach number, 0.60. Although the overall level is the same at  $M = 0.60$  and 9.00, because of the narrower bandwidth at subsonic Mach numbers a structural mode that falls within the  $M = 0.60$  band would be subject to a larger input than would any mode at  $M = 9.00$ . Also, the higher correlation at the lower Mach numbers, as shown in figure 21, would make the input more effective at  $M = 0.60$ . However, if the pressure fluctuations follow the usual scaling assumption that the overall FPL remains constant and the frequency varies inversely with the ratio full-scale length/model length, the input frequencies would be very low ( $B < 5$  Hz for a scale factor of 10) at subsonic Mach numbers. It should be possible to design even a fragile structure so that its modes would fall above such low input frequencies and respond only to the less severe loading at the higher Mach numbers.

#### CONCLUDING REMARKS

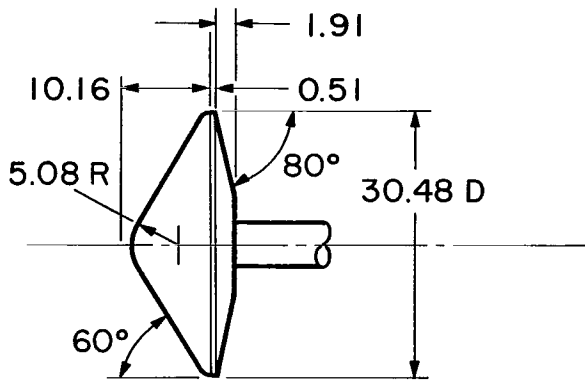
Pressure fluctuations measured on the afterbodies of five blunt entry configurations showed little effect due to changes in afterbody angle from  $30^\circ$  to  $80^\circ$ . At subsonic Mach numbers the Strouhal number of the fluctuations was less than 0.30 but increased with Mach number to about 0.74 at  $M = 3.00$ . There was a high degree of spatial correlation along the afterbodies at subsonic Mach numbers and small angles of attack. Correlation decreased with increasing Mach number and angle of attack.

Estimates were made of the fluctuating pressure level that might be encountered in entering the VM3 Mars atmosphere from a 244 km orbit. They indicated that the maximum level would be about 115 dB for  $M/C_{DA} = 62 \text{ kg/m}^2$ .

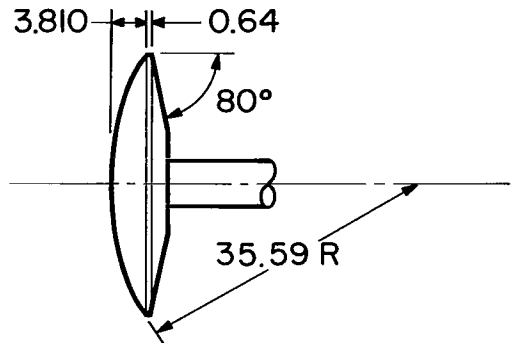
Ames Research Center  
National Aeronautics and Space Administration  
Moffett Field, Calif., 94035, Feb. 29, 1968  
124-08-04-04-00-21

## REFERENCES

1. Seiff, Alvin: Developments in Entry Vehicle Technology. AIAA Paper 64-528, 1964.
2. Roberts, Leonard: Entry Into Planetary Atmospheres. *Astronautics and Aeronautics*, vol. 2, no. 10, Oct. 1964, pp. 22-29.
3. Bendat, J. S.; and Piersol, A. G.: *Measurement and Analysis of Random Data*. John Wiley and Sons, N. Y., 1966.
4. Bendat, Julius S.; Enochson, L. D.; Klein, G. H.; and Piersol, A. G.: *The Application of Statistics to the Flight Vehicle Vibration Problem*. ASD TR 61-123, Aeronautical Systems Division, AFSC, Wright-Patterson AFB, Ohio, Dec. 1961.
5. Crandall, Steven H., et al.: *Random Vibration*. The Technology Press of MIT, Cambridge, Mass., 1958.
6. Fung, Y. C.: *An Introduction to the Theory of Aeroelasticity*. John Wiley and Sons, N. Y., 1955.
7. Georgiev, Steven: *A Feasibility Study of an Experiment for Determining the Properties of the Mars Atmosphere*. Vol. 1, Summary. NASA CR-530, 1967.

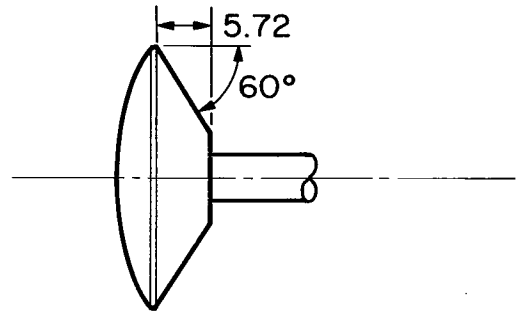


Model A

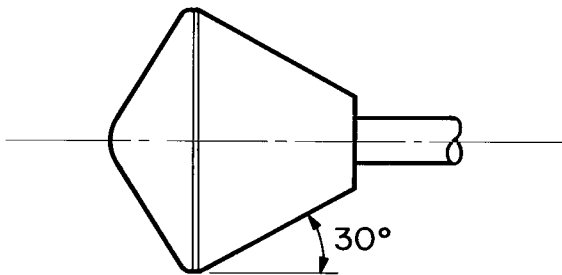


Model C

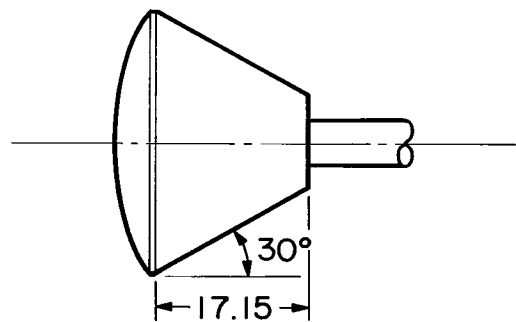
Note: All dimensions in centimeters



Model D



Model B



Model E

Figure 1.- Model configuration.

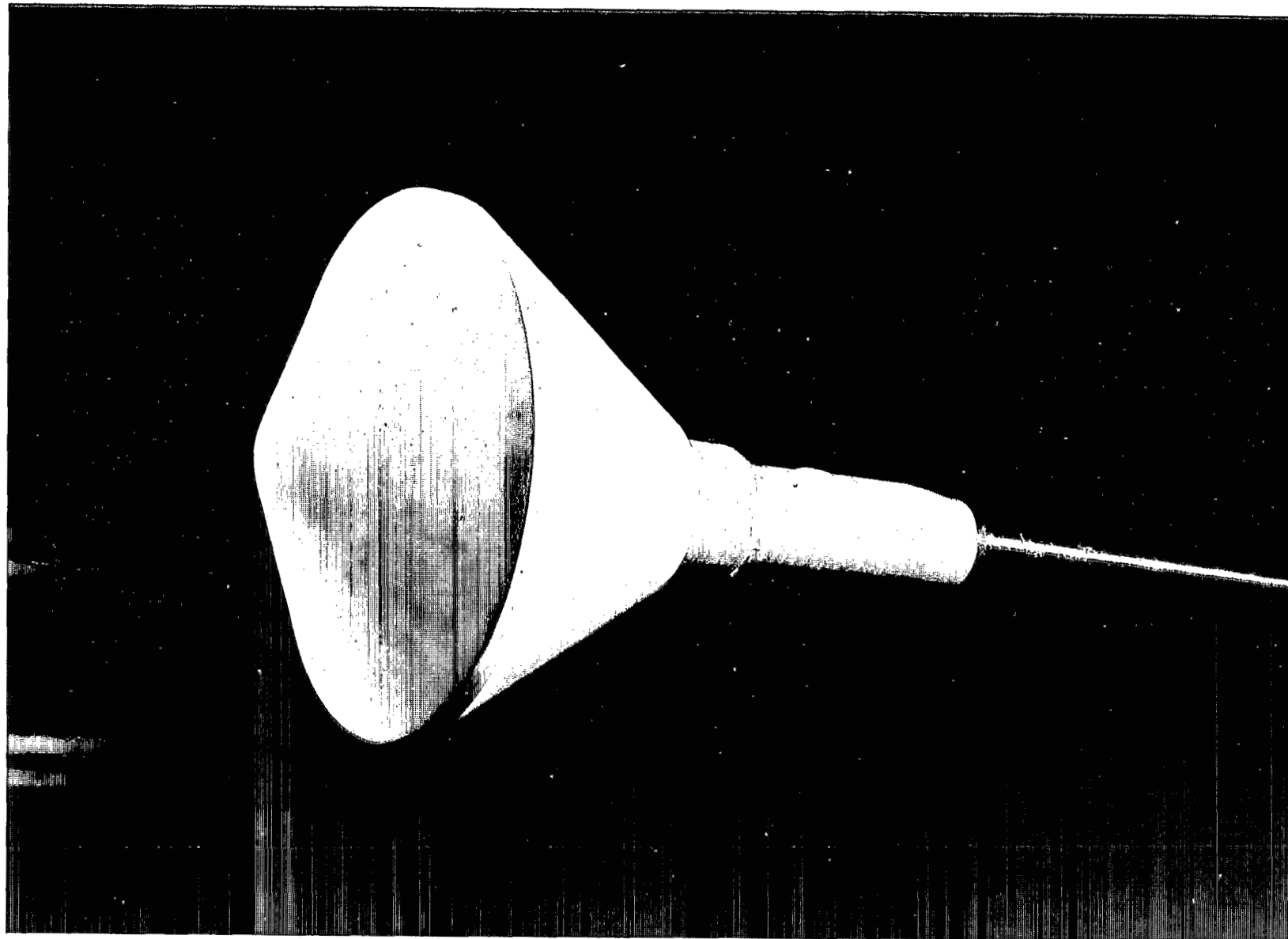
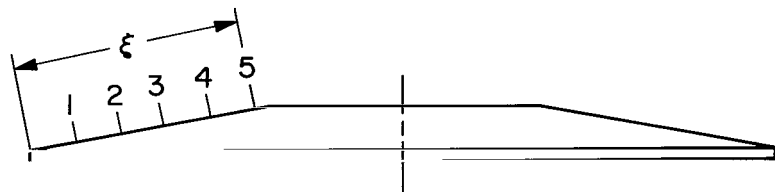
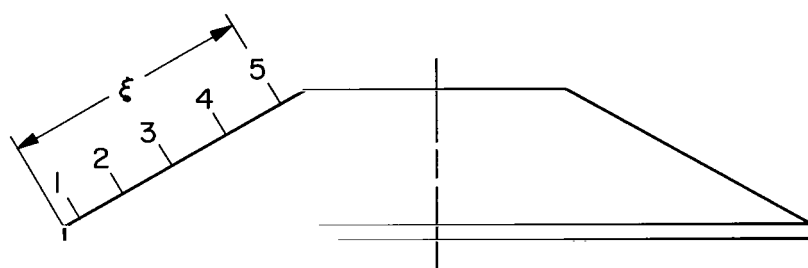


Figure 2.- Model B in the 11- by 11-foot wind tunnel.



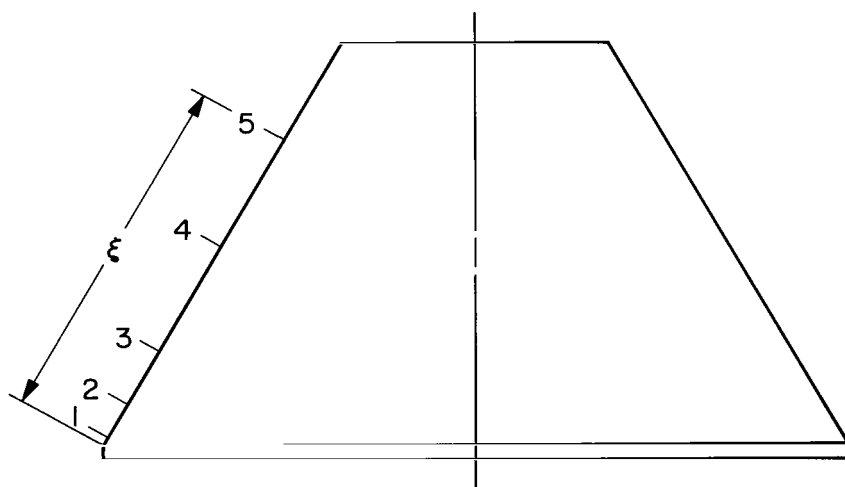
(a) 80° Afterbody

Static orifice and P. T.	$\xi$ , cm
1	1.91
2	3.81
3	5.56
4	7.62
5	9.37



(b) 60° Afterbody

Static orifice and P. T.	$\xi$ , cm
1	0.40
2	2.30
3	4.84
4	7.38
5	9.92



(c) 30° Afterbody

Static orifice and P. T.	$\xi$ , cm
1	0.32
2	1.91
3	4.45
4	9.53
5	14.61

Figure 3.- Location of the pressure transducers and the corresponding static pressure orifices.

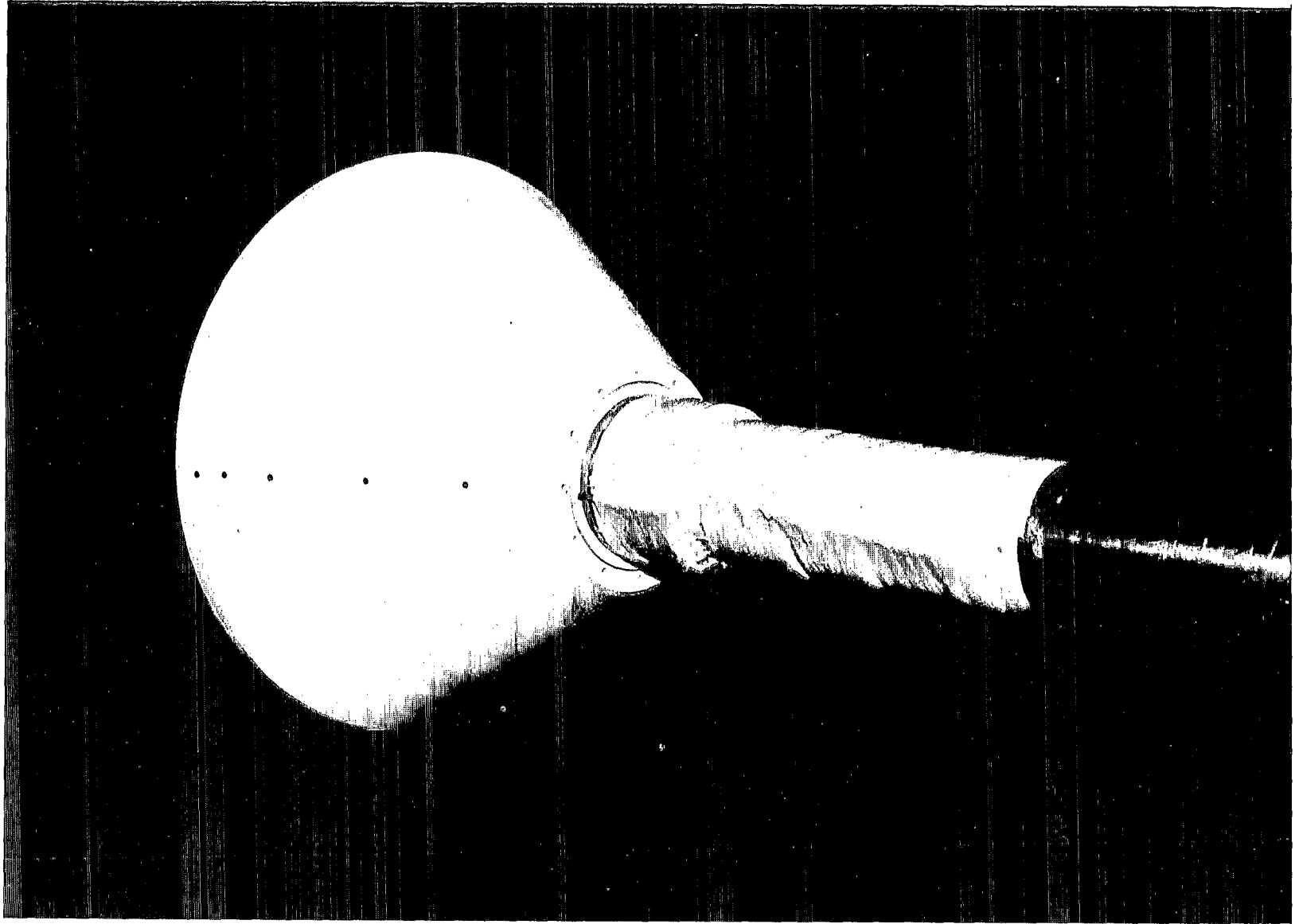
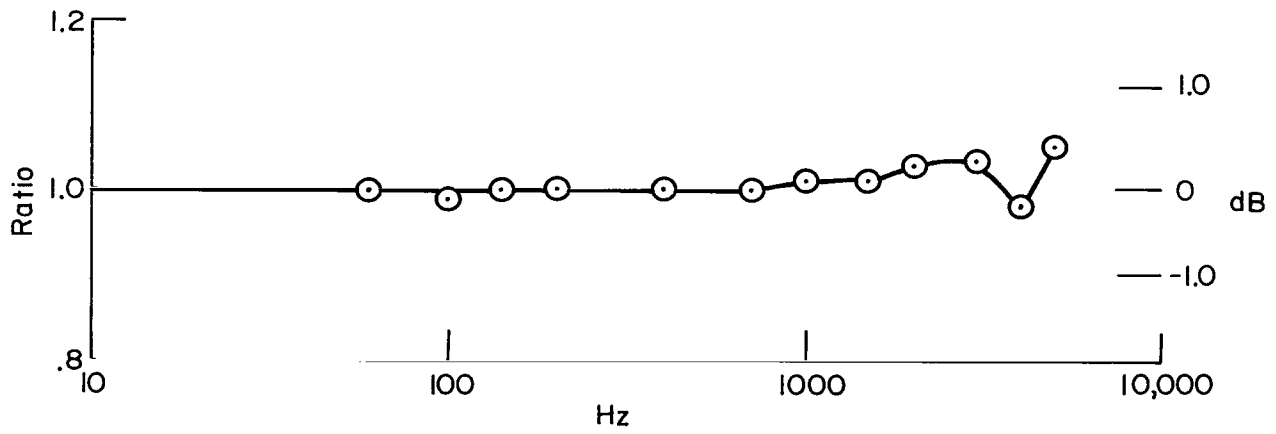
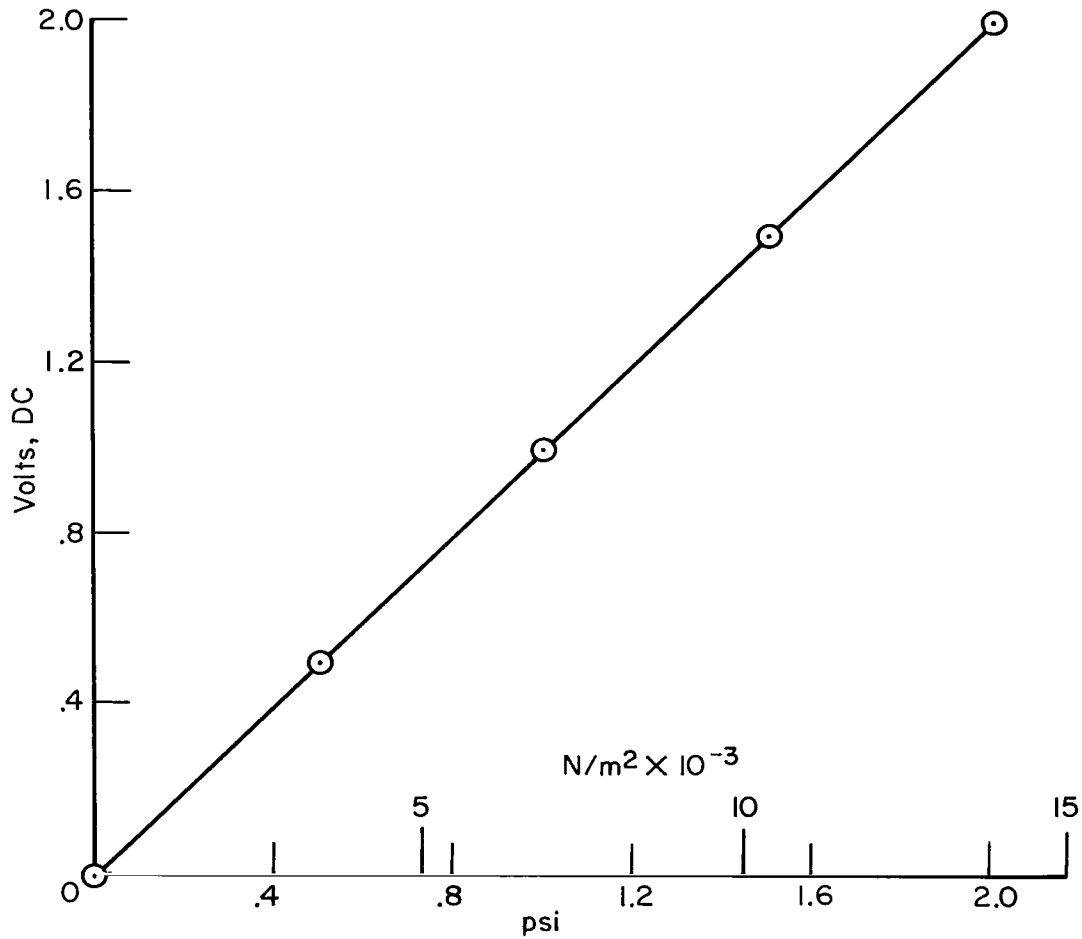


Figure 4.- Pressure transducers mounted in the  $30^\circ$  afterbody.

A-36472



(a) Frequency response.



(b) Static calibration.

Figure 5.- Characteristics of a typical pressure transducer.



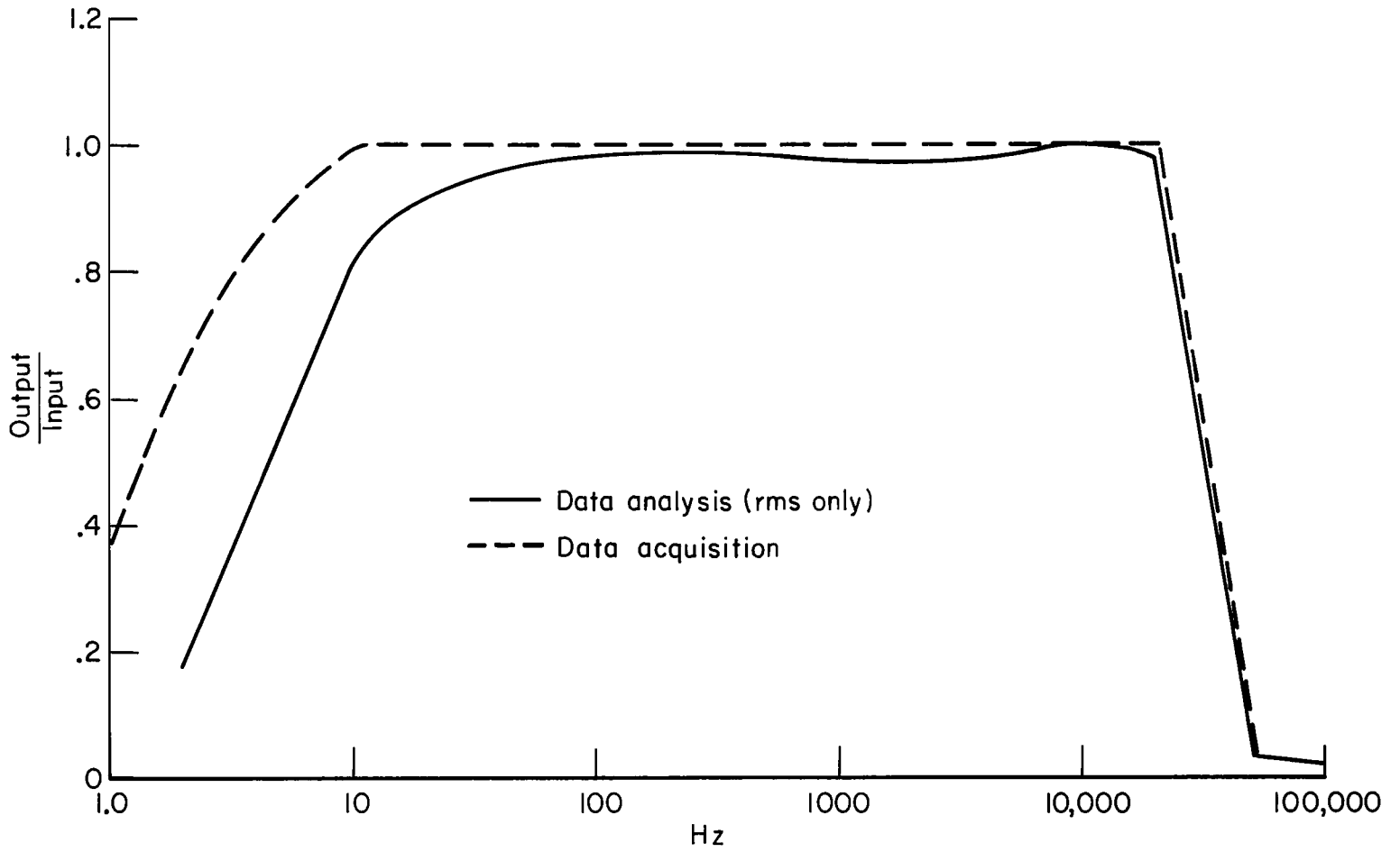


Figure 7.- Frequency response of the data acquisition and analysis systems.

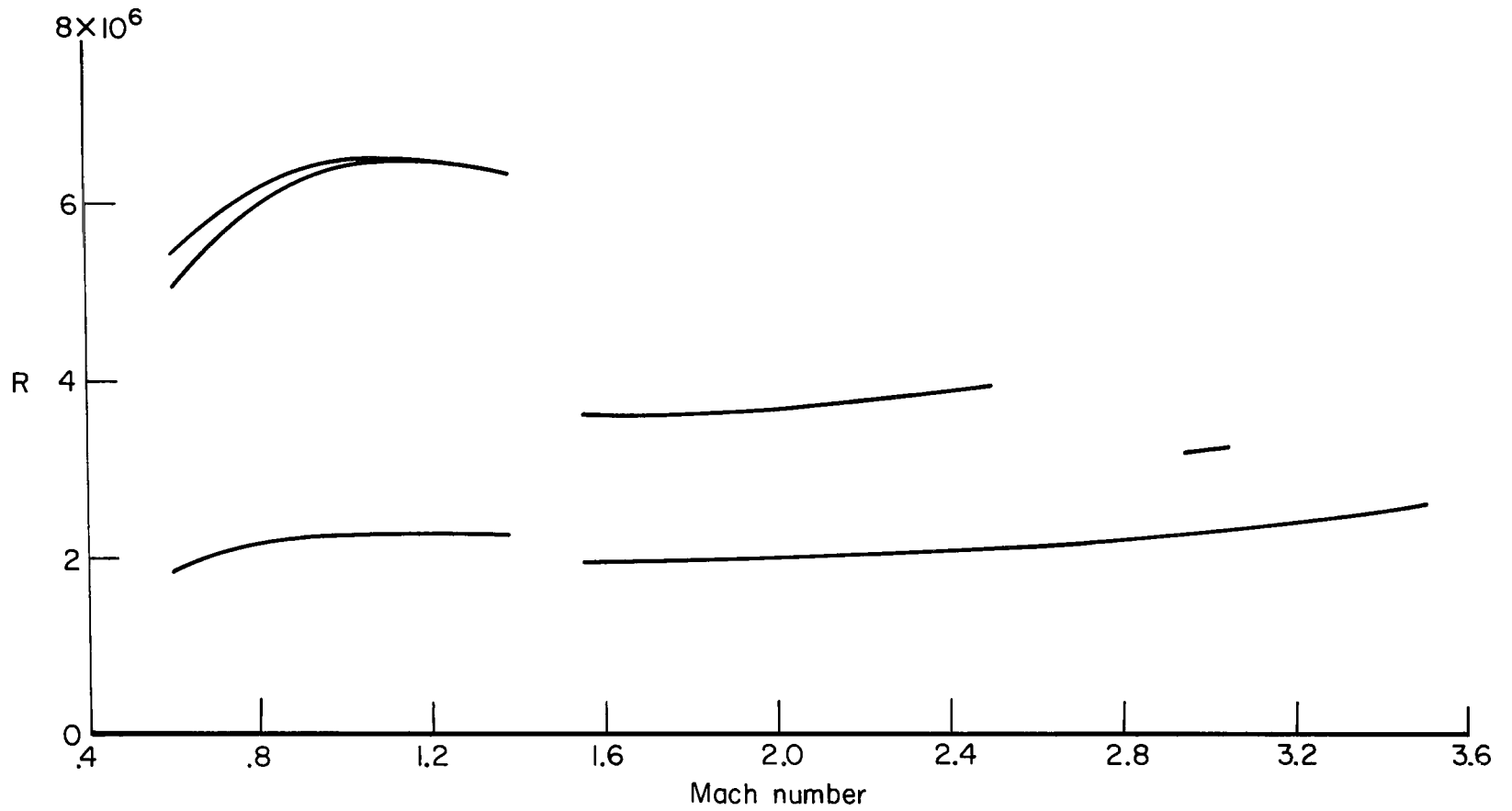
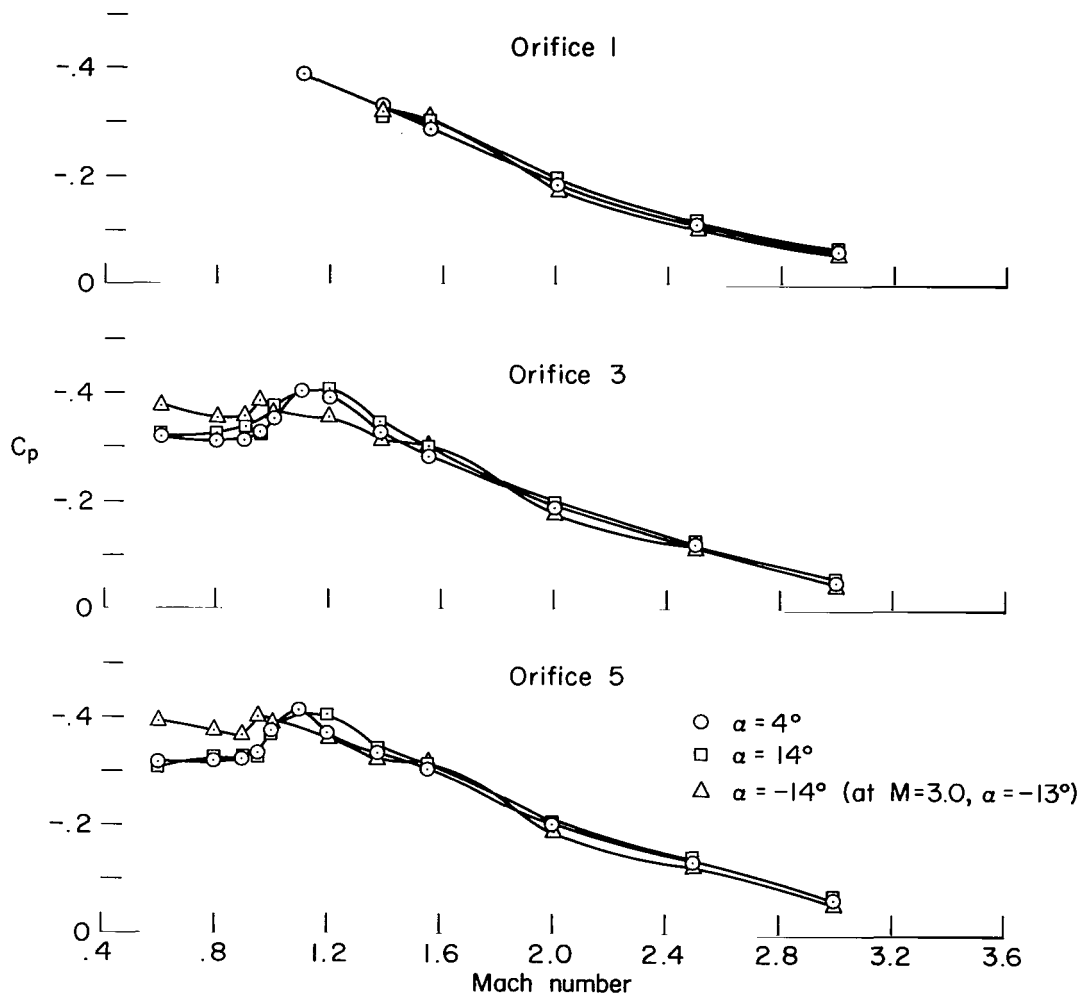
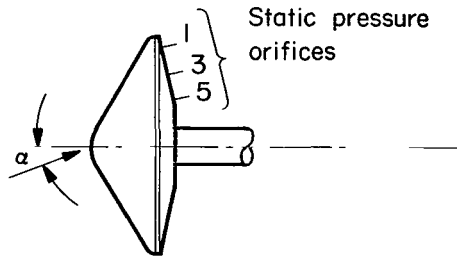
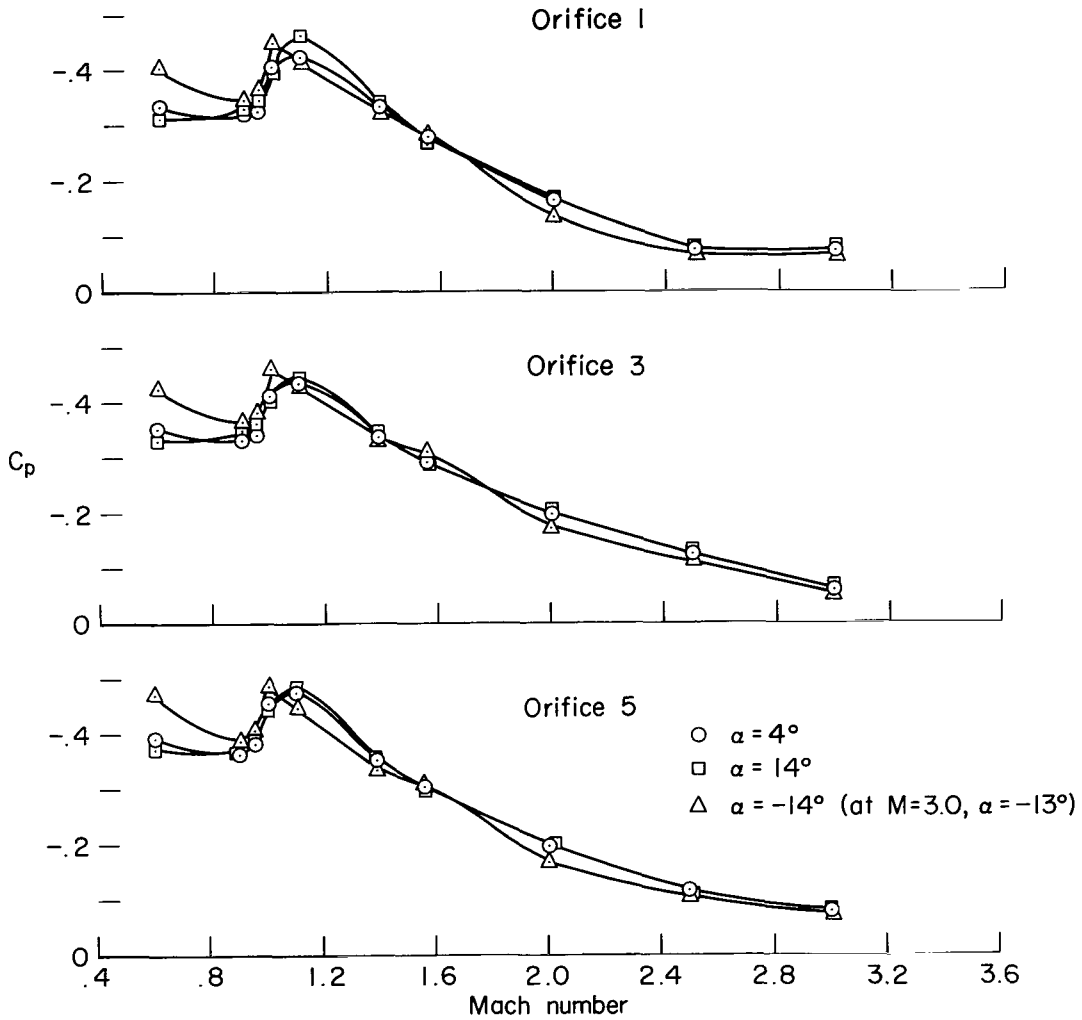
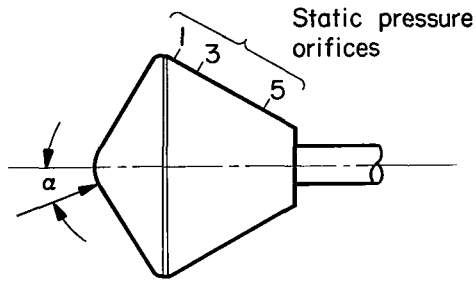


Figure 8.- Reynolds numbers for the tests, based on model diameter.



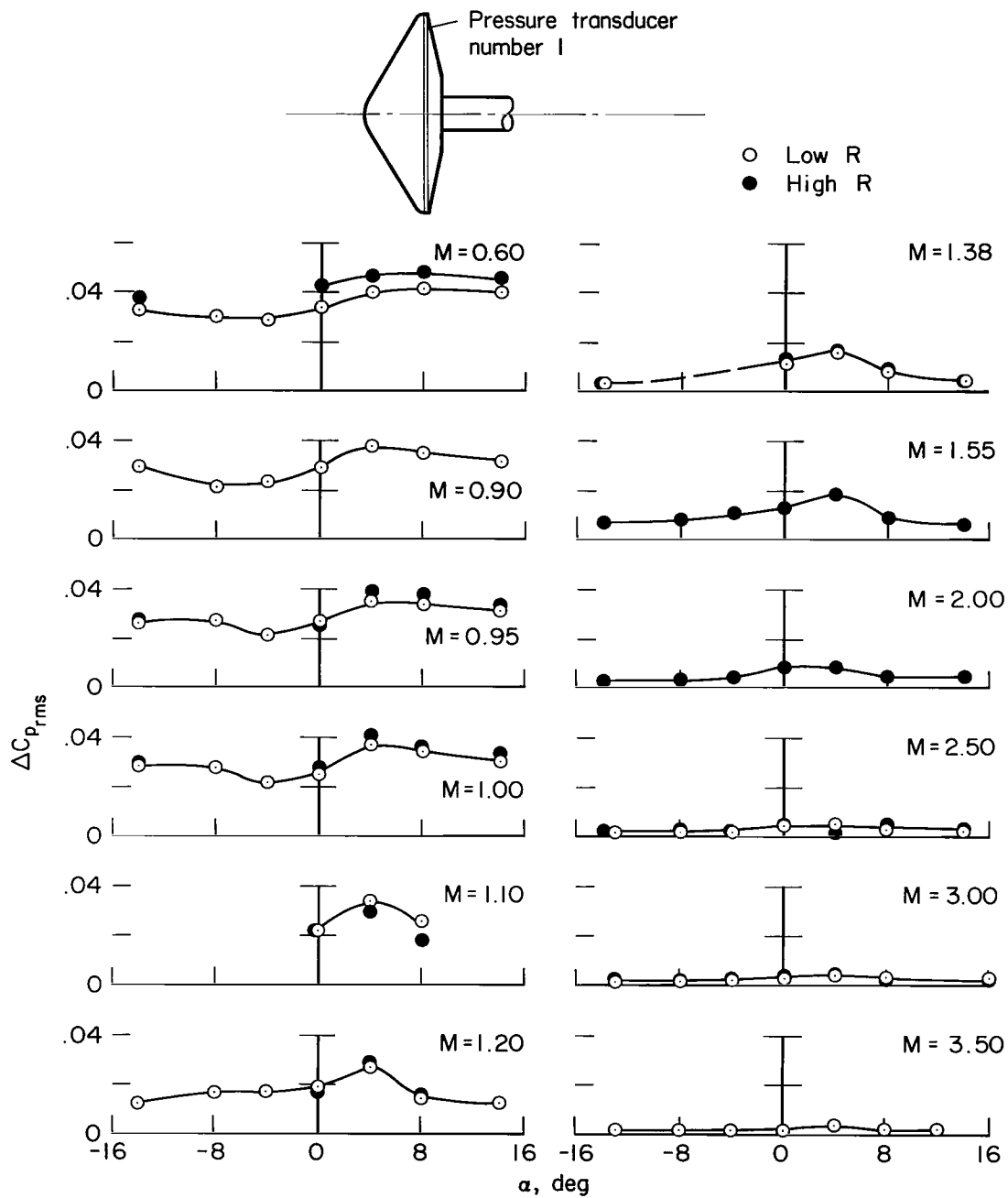
(a) Model A

Figure 9.- The effect of Mach number on the static pressure.



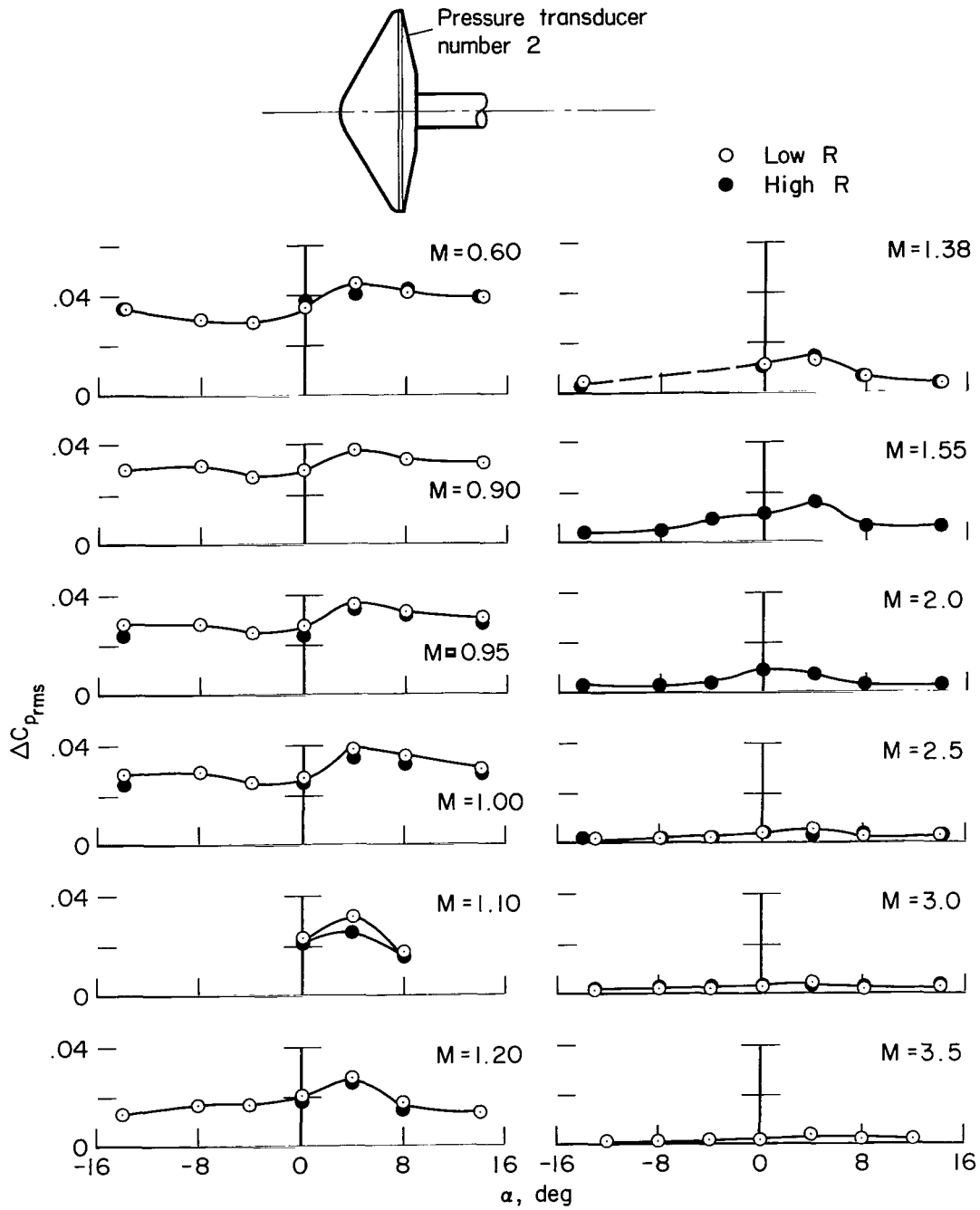
(b) Model B

Figure 9.- Concluded.



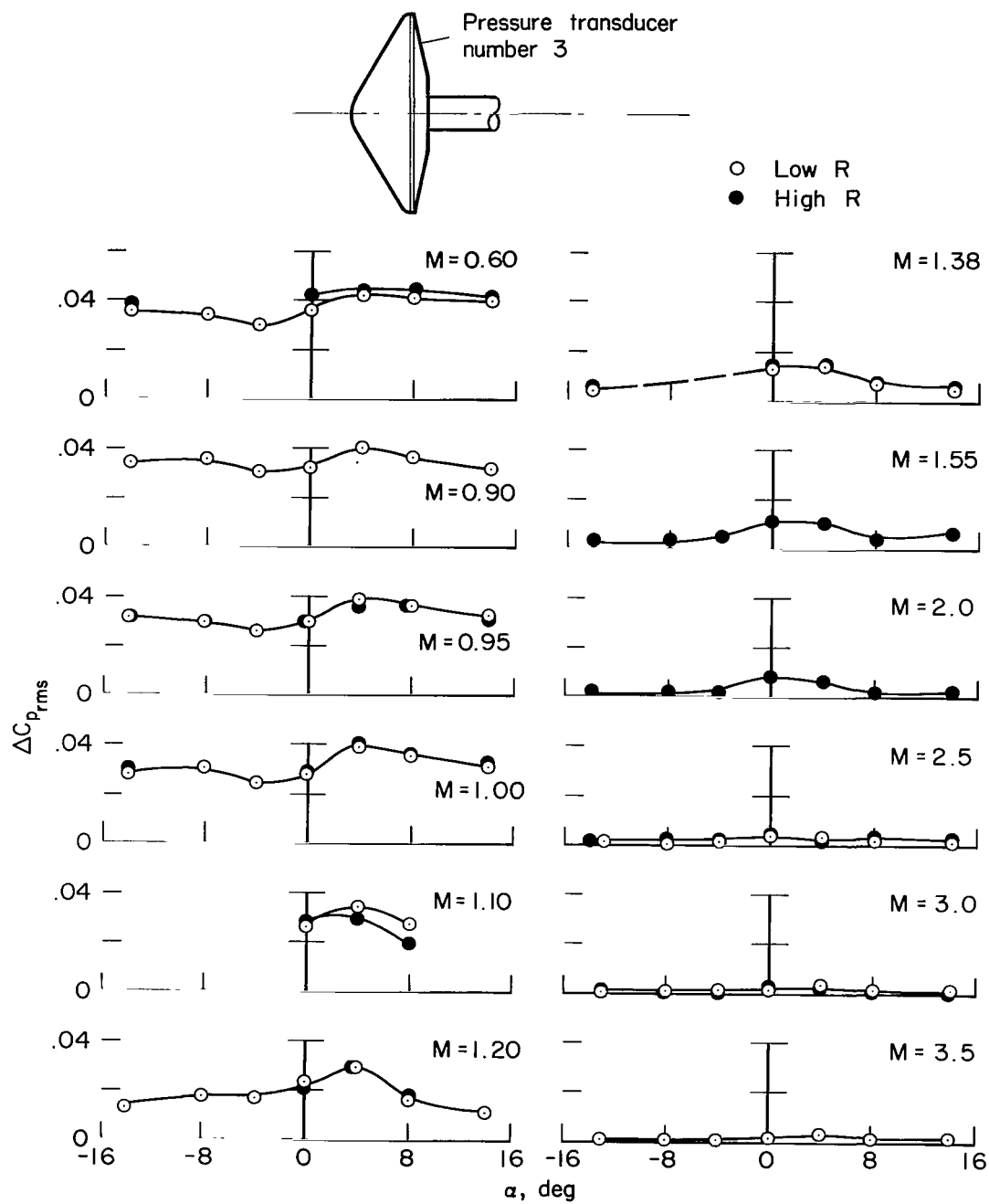
(a) Pressure transducer number 1.

Figure 10.- Pressure fluctuations on model A.



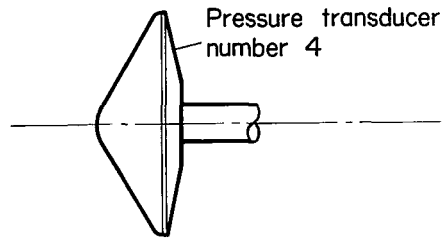
(b) Pressure transducer number 2.

Figure 10.- Continued.

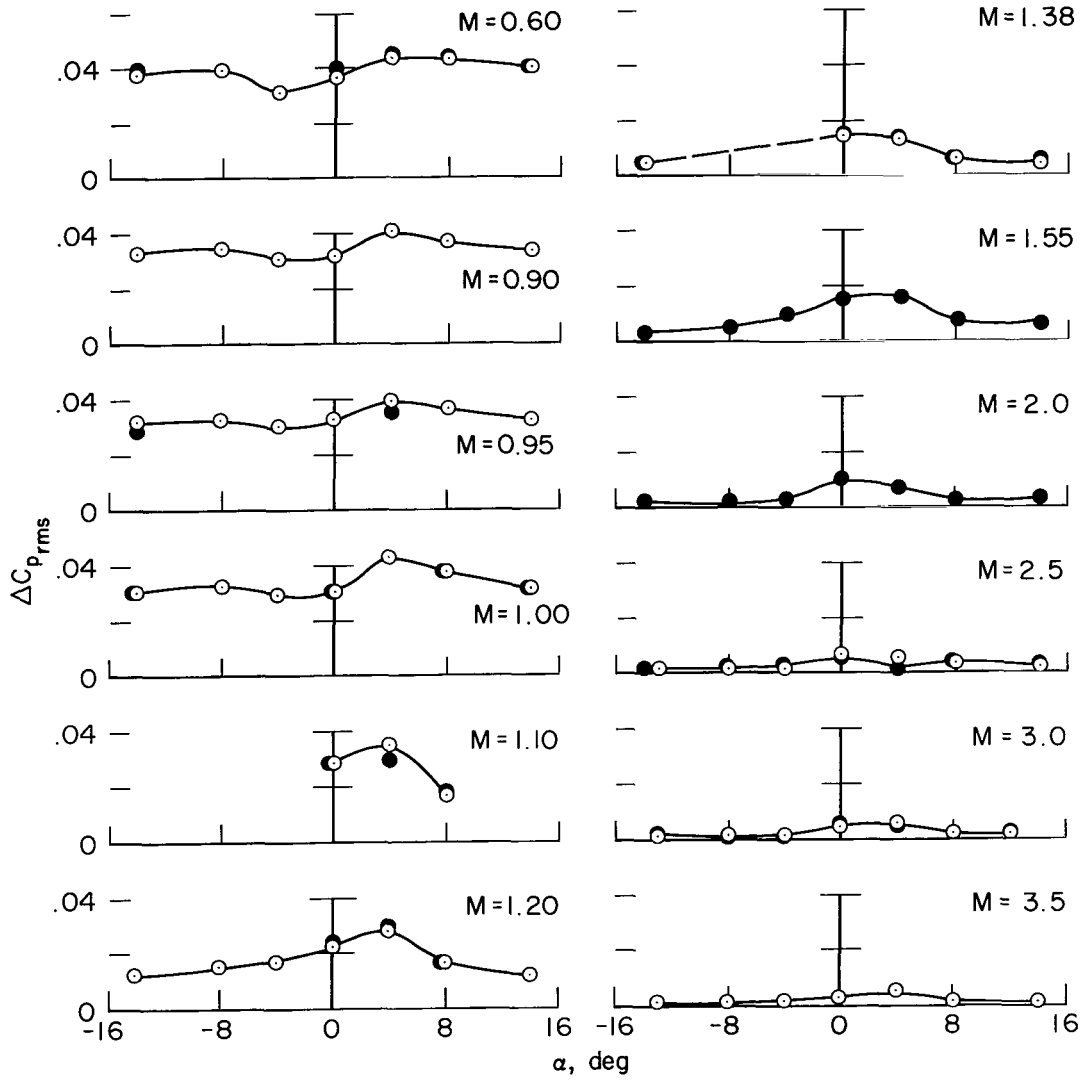


(c) Pressure transducer number 3.

Figure 10.- Continued.

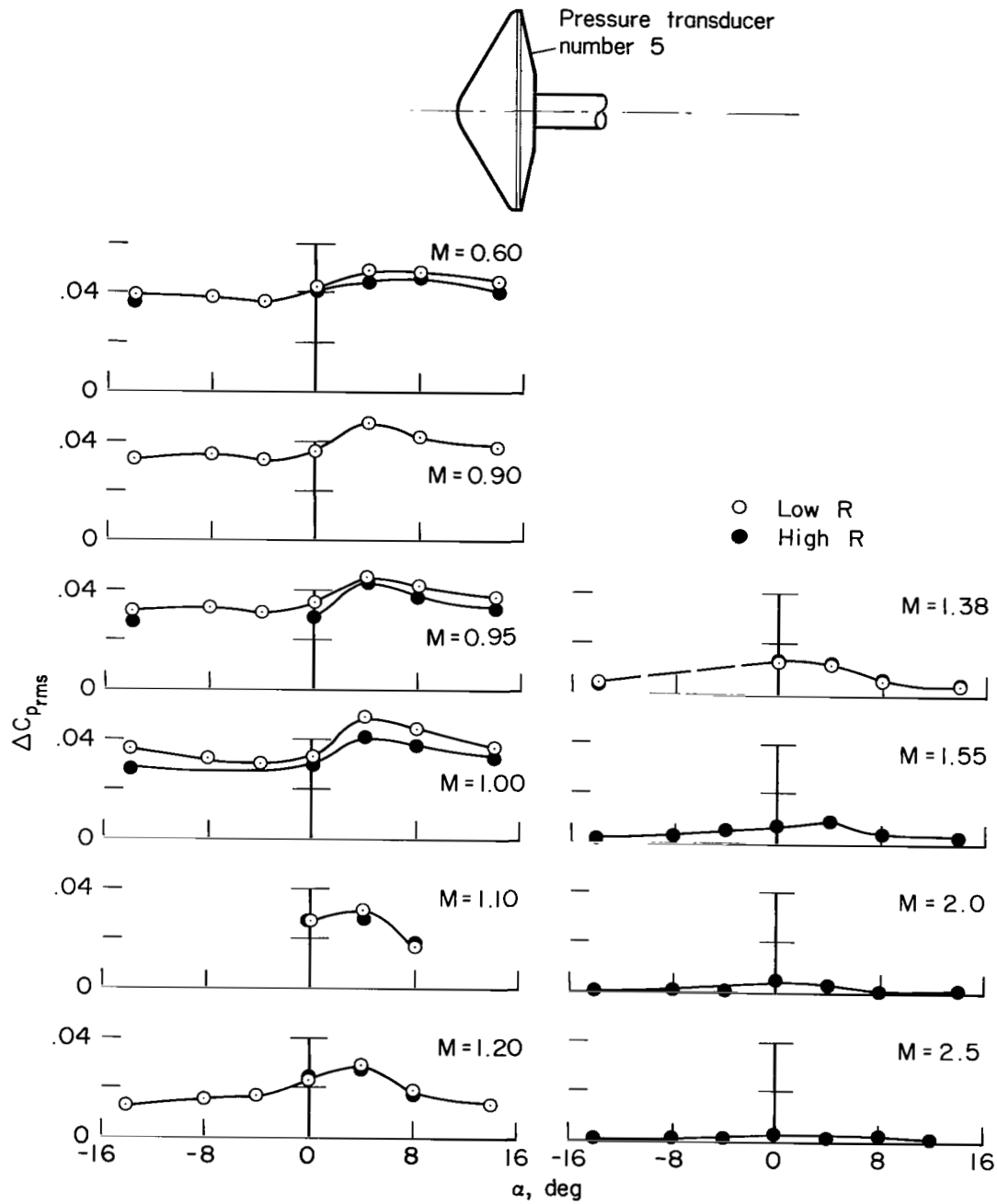


○ Low R  
● High R



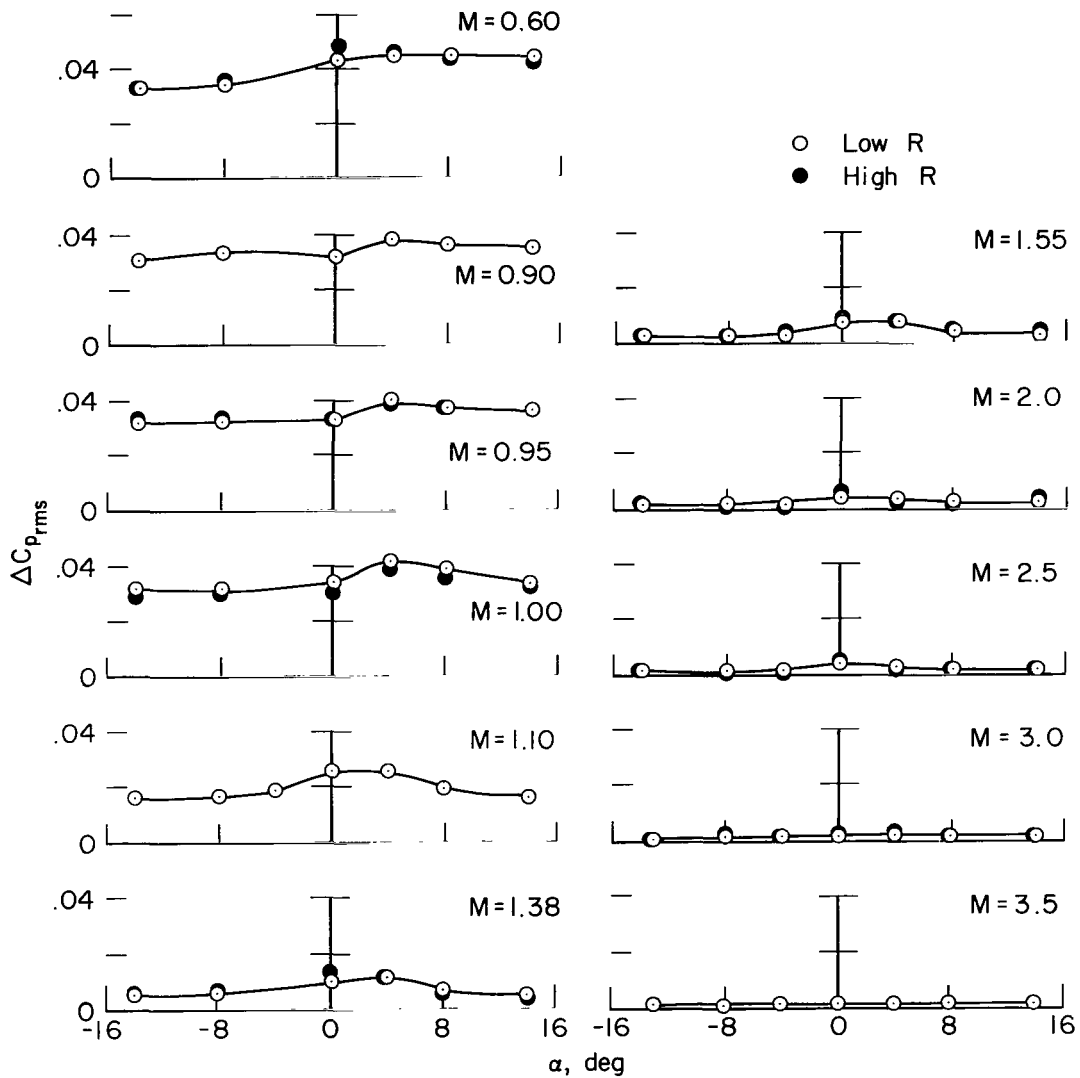
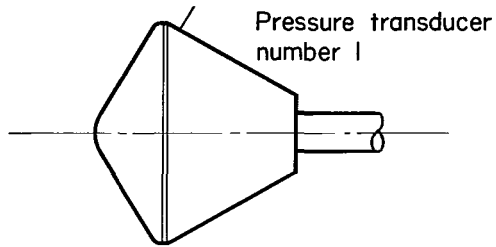
(d) Pressure transducer number 4.

Figure 10.- Continued.



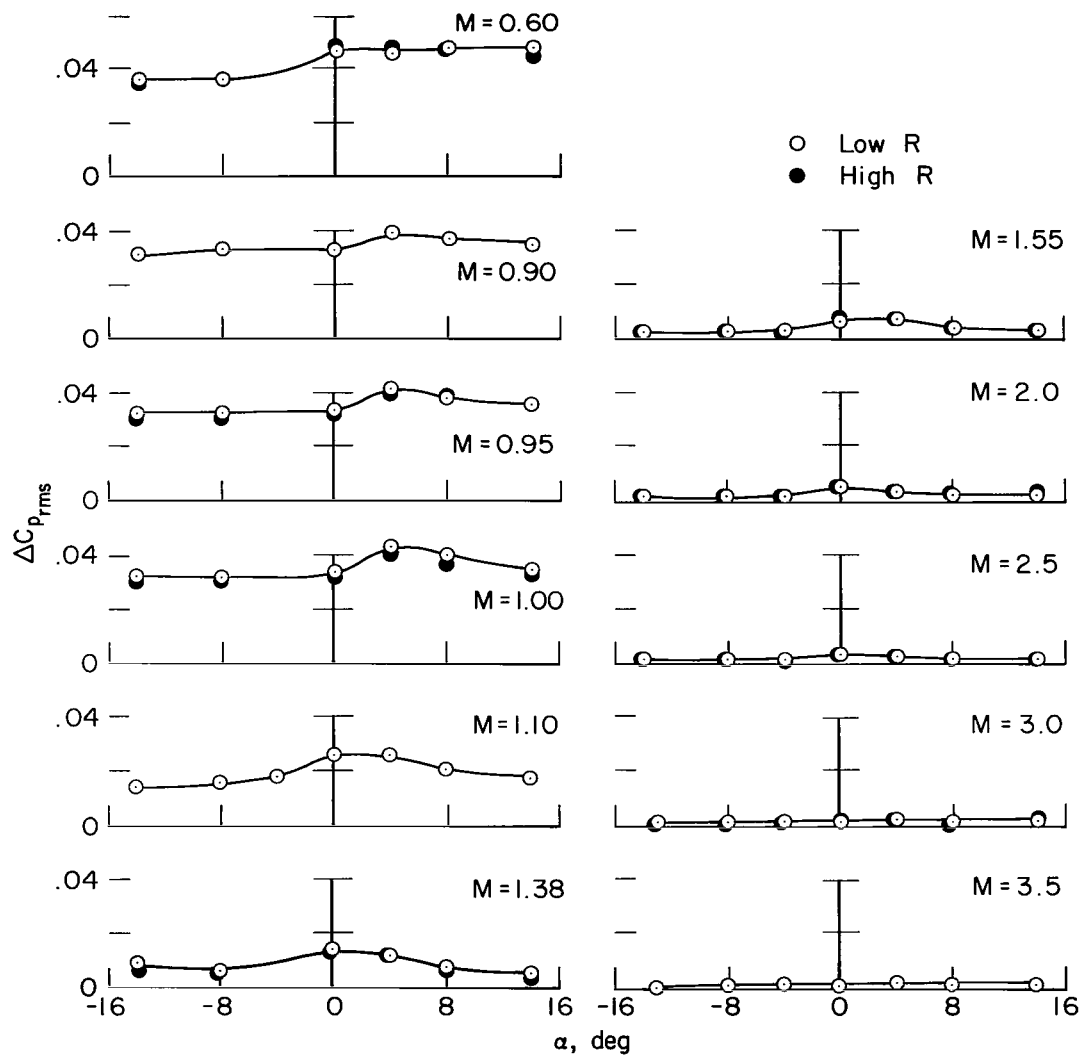
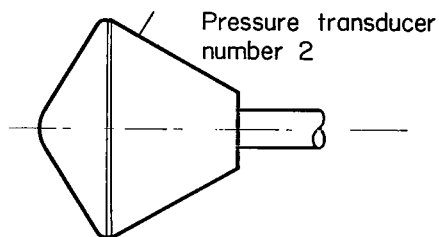
(e) Pressure transducer number 5.

Figure 10.- Concluded.



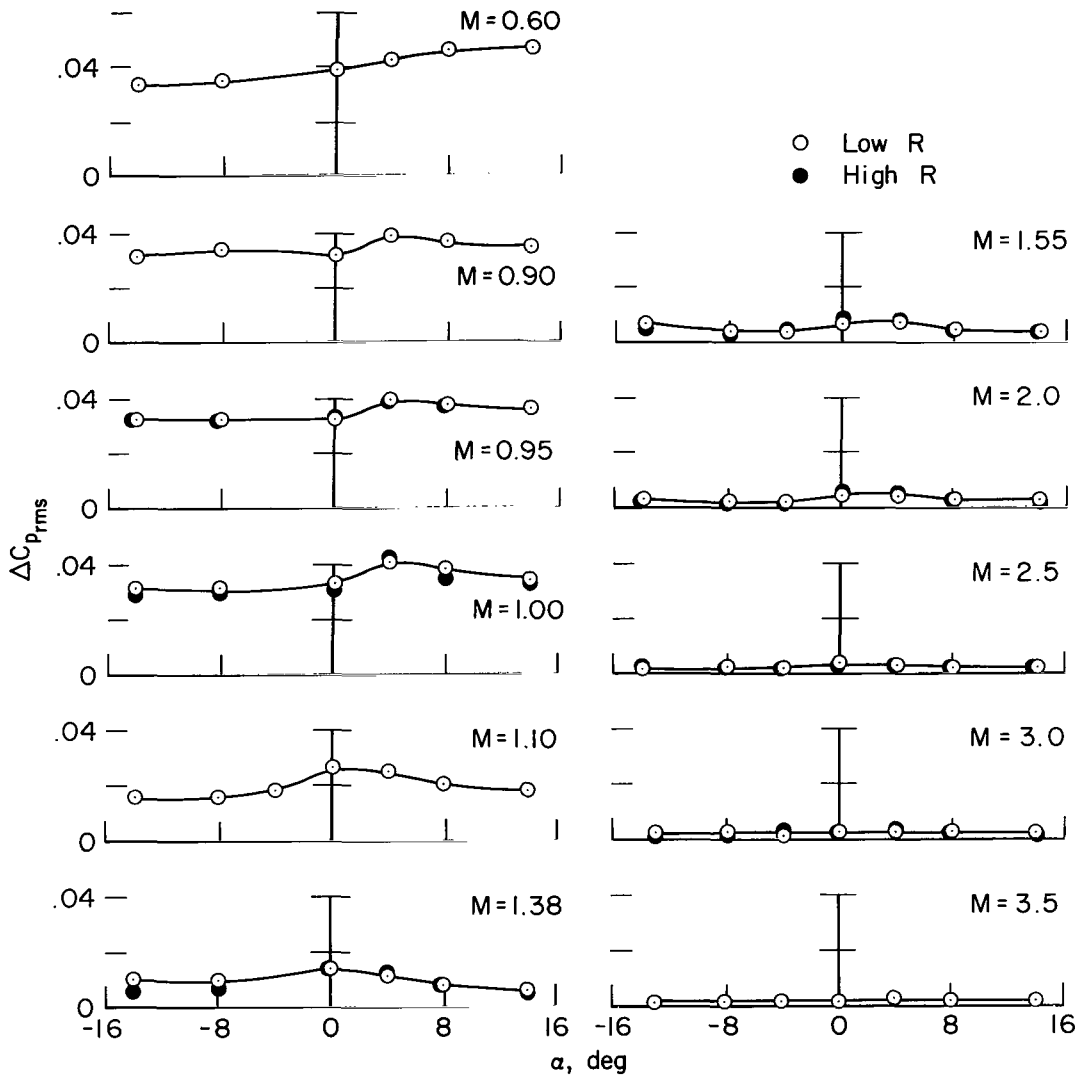
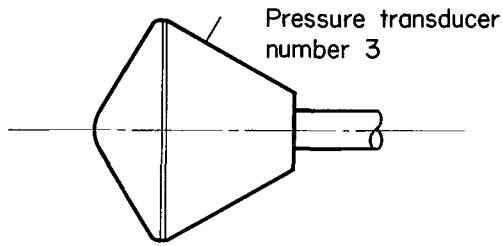
(a) Pressure transducer number 1.

Figure 11.- Pressure fluctuations on model B.



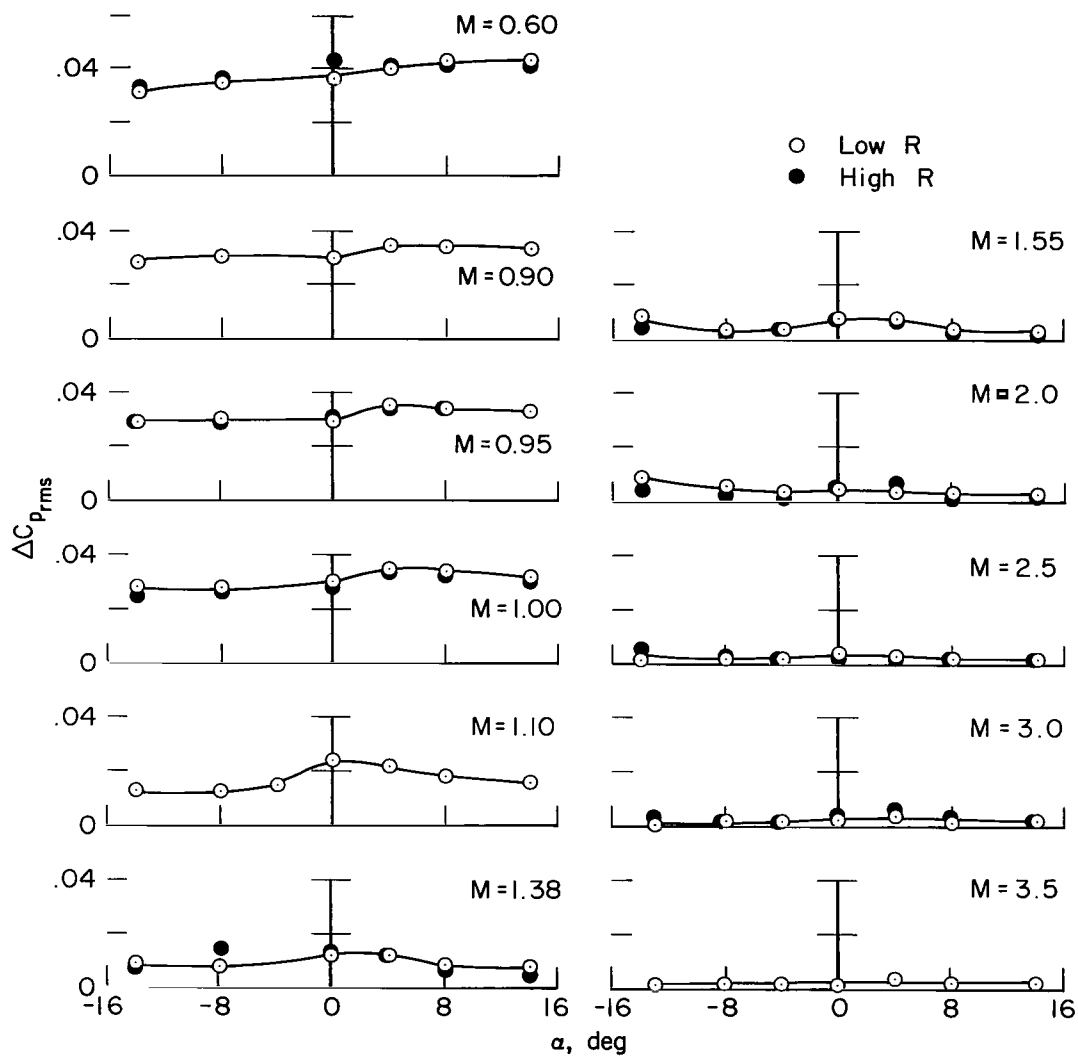
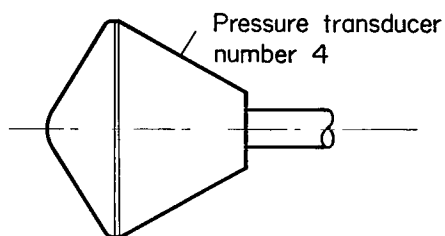
(b) Pressure transducer number 2.

Figure 11.- Continued.



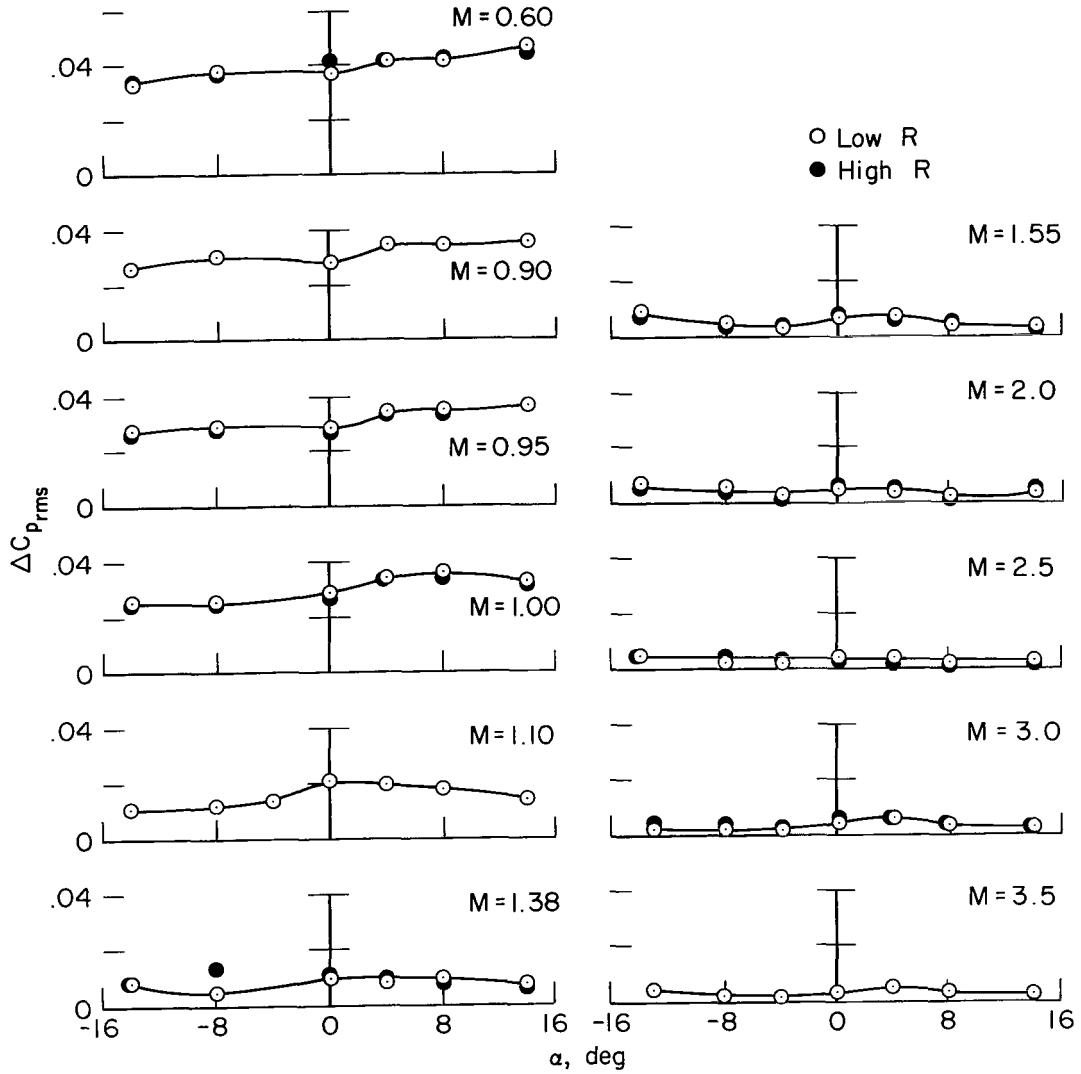
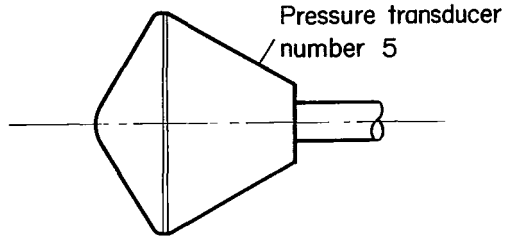
(c) Pressure transducer number 3.

Figure 11.- Continued.



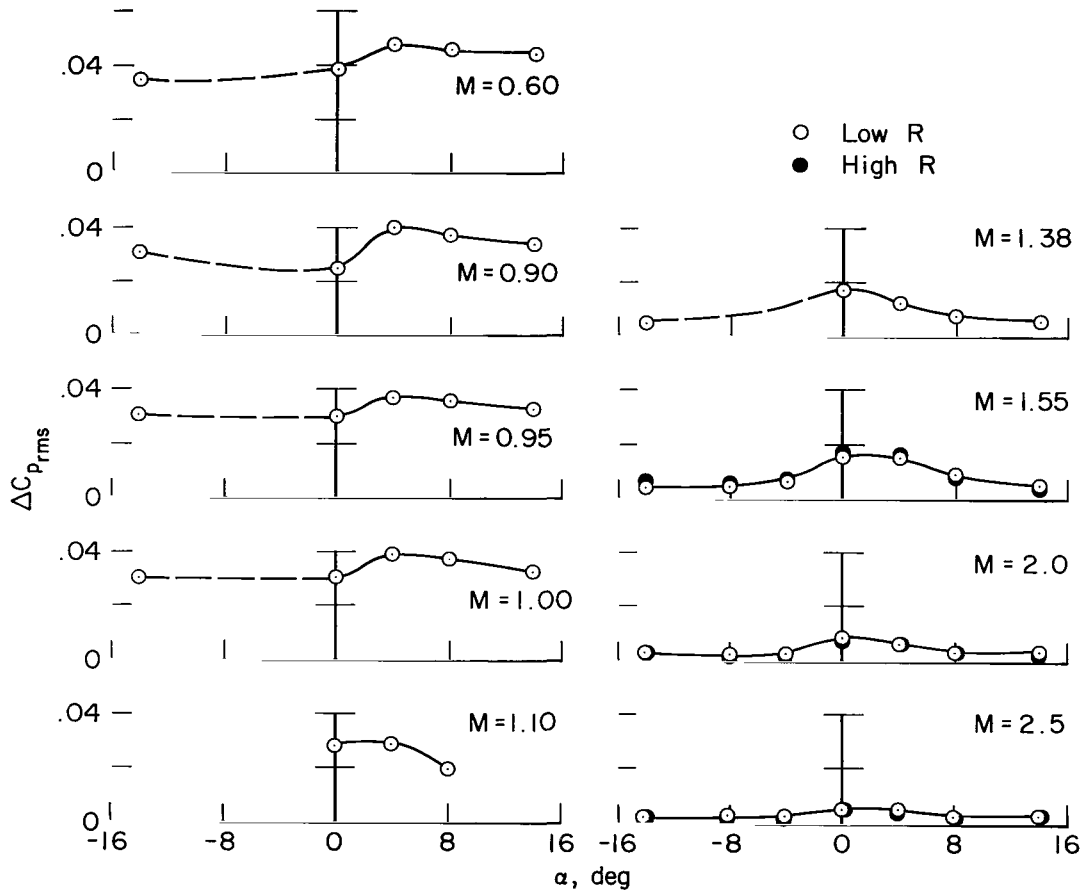
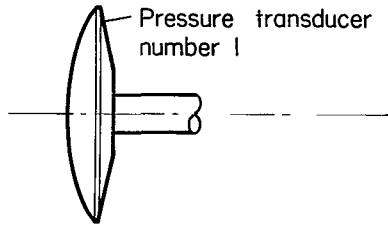
(d) Pressure transducer number 4.

Figure 11.- Continued.



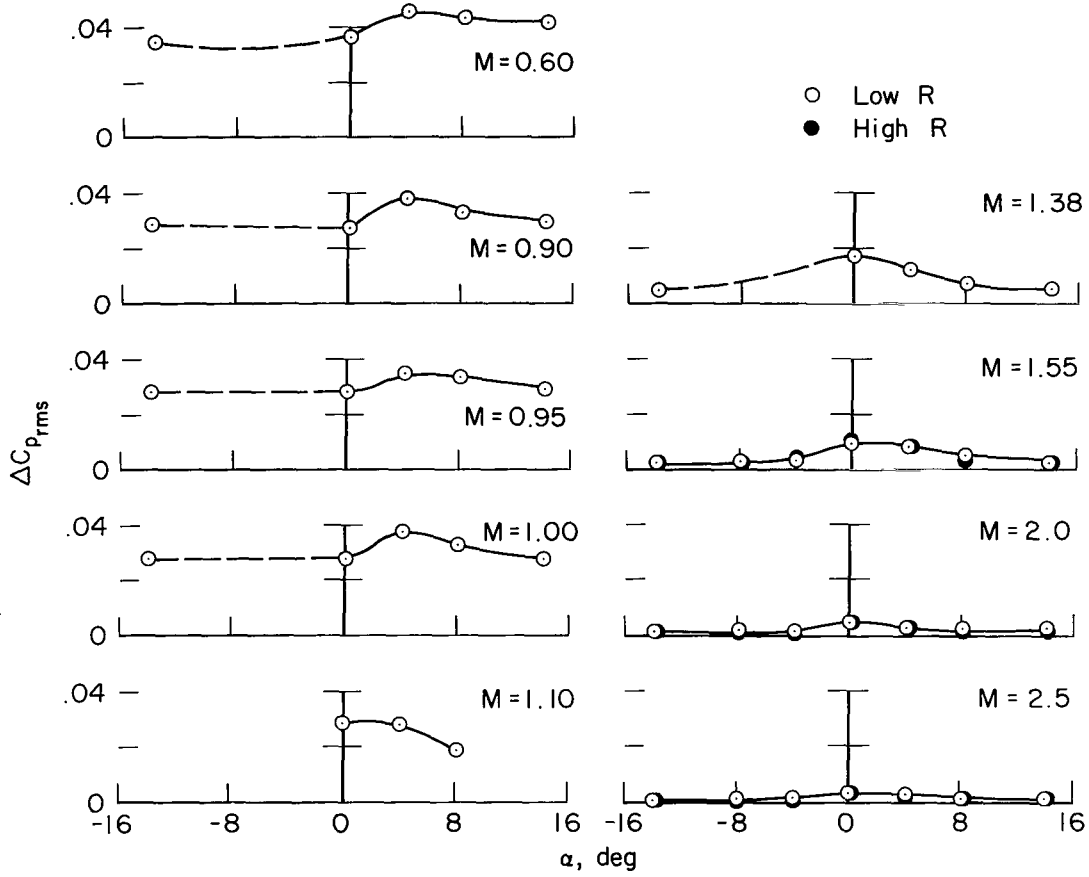
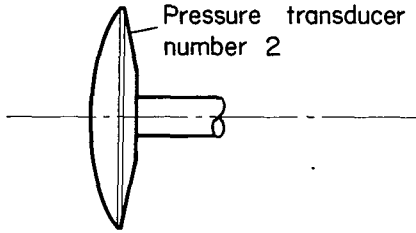
(e) Pressure transducer number 5.

Figure 11.- Concluded.



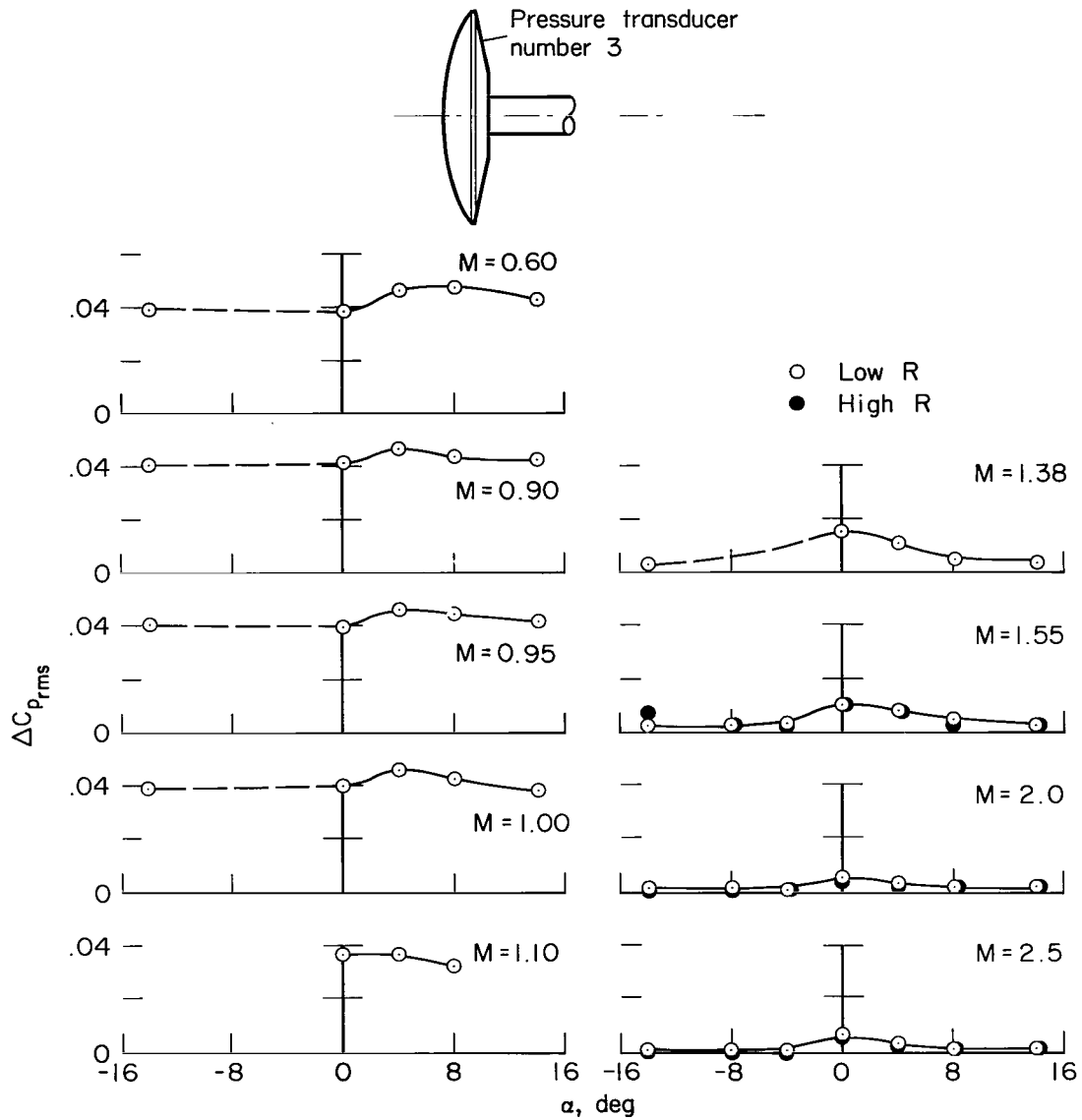
(a) Pressure transducer number 1.

Figure 12.- Pressure fluctuations on model C.



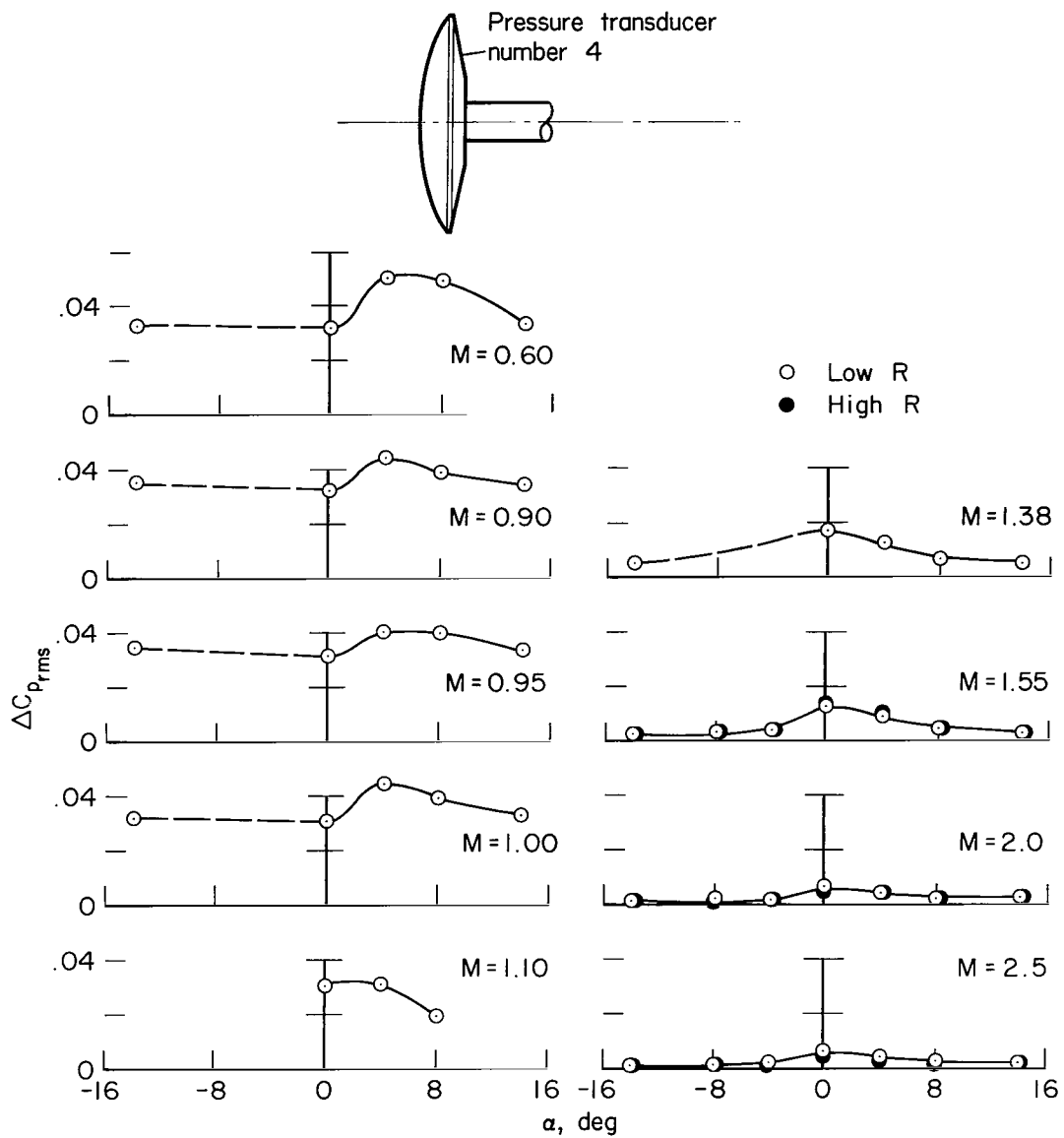
(b) Pressure transducer number 2.

Figure 12.- Continued.



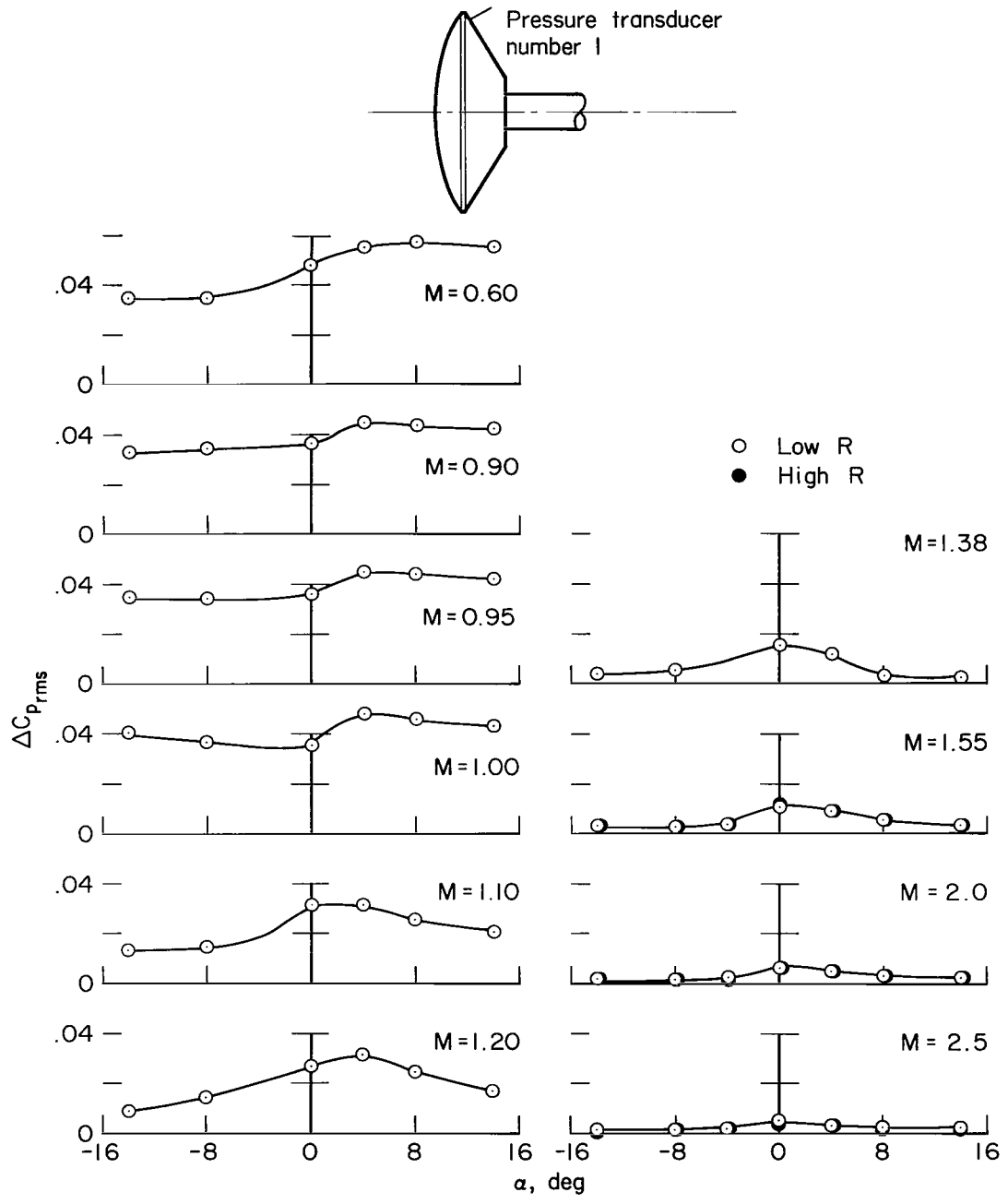
(c) Pressure transducer number 3.

Figure 12.- Continued.



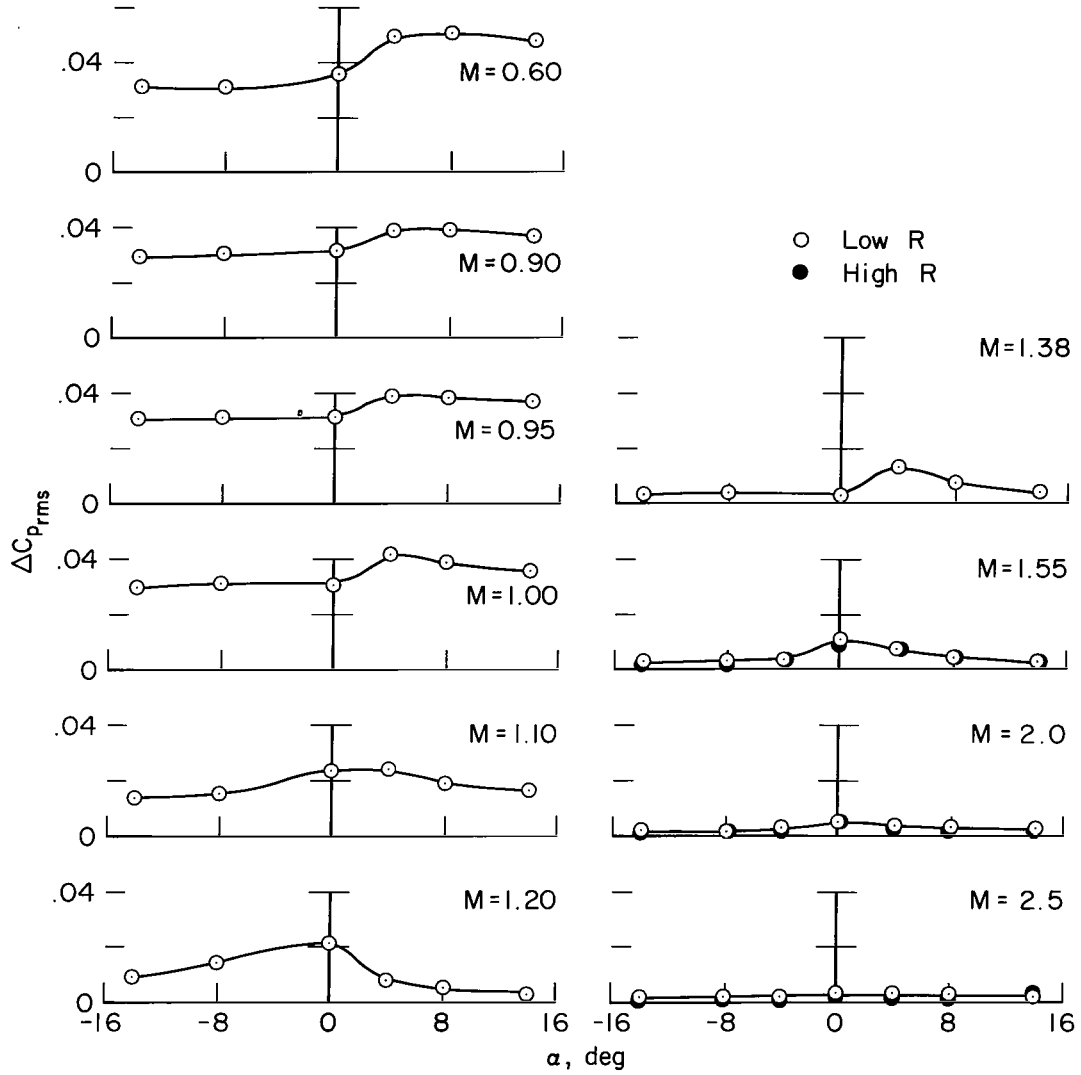
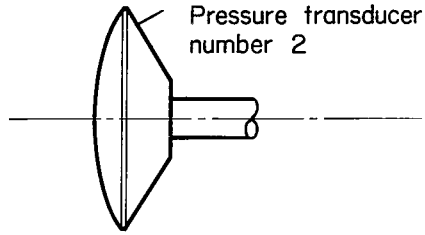
(d) Pressure transducer number 4.

Figure 12.- Concluded.



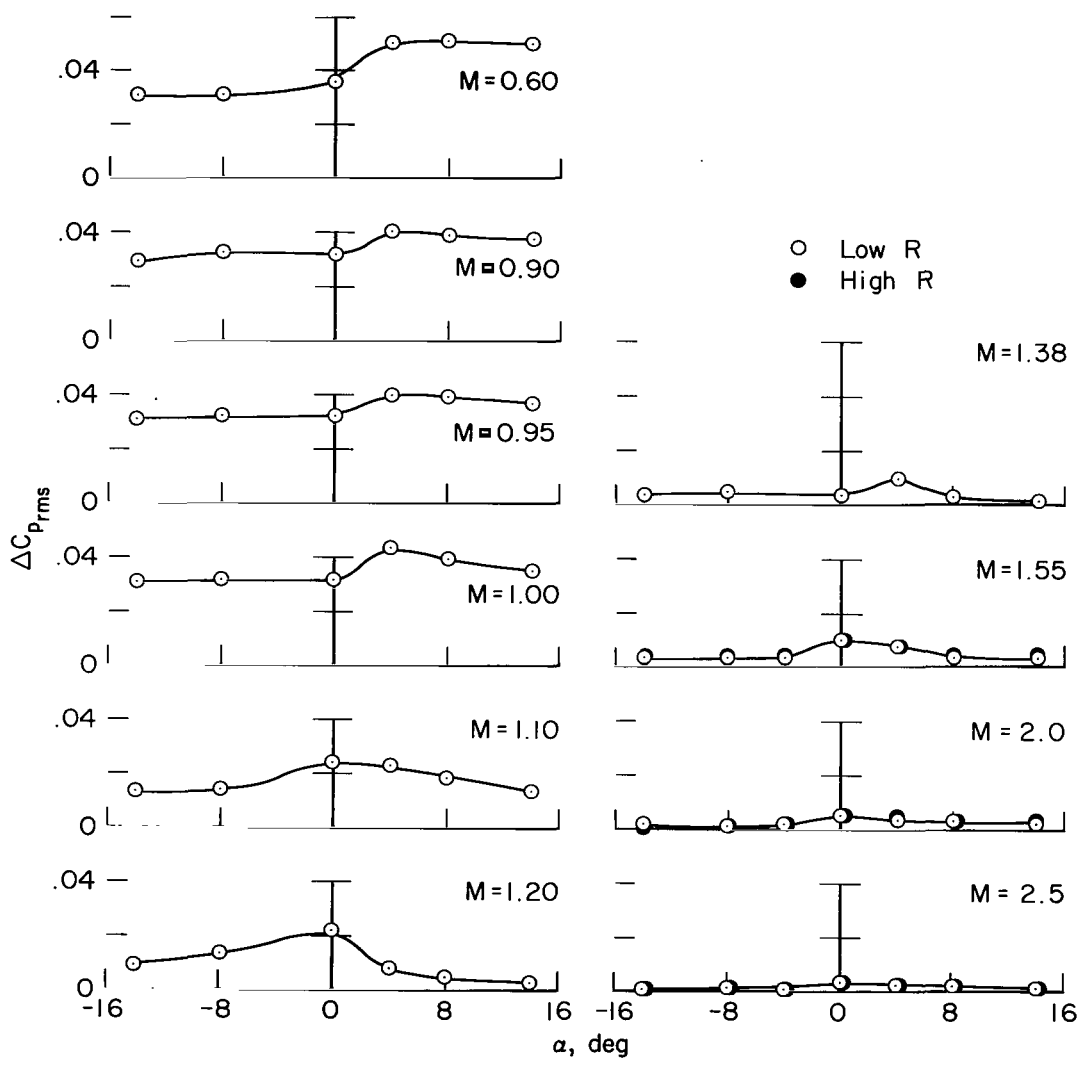
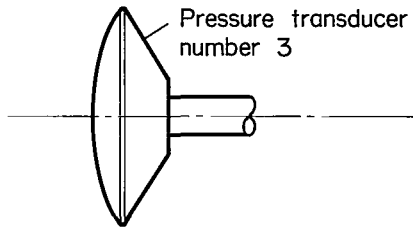
(a) Pressure transducer number 1.

Figure 13.- Pressure fluctuations on model D.



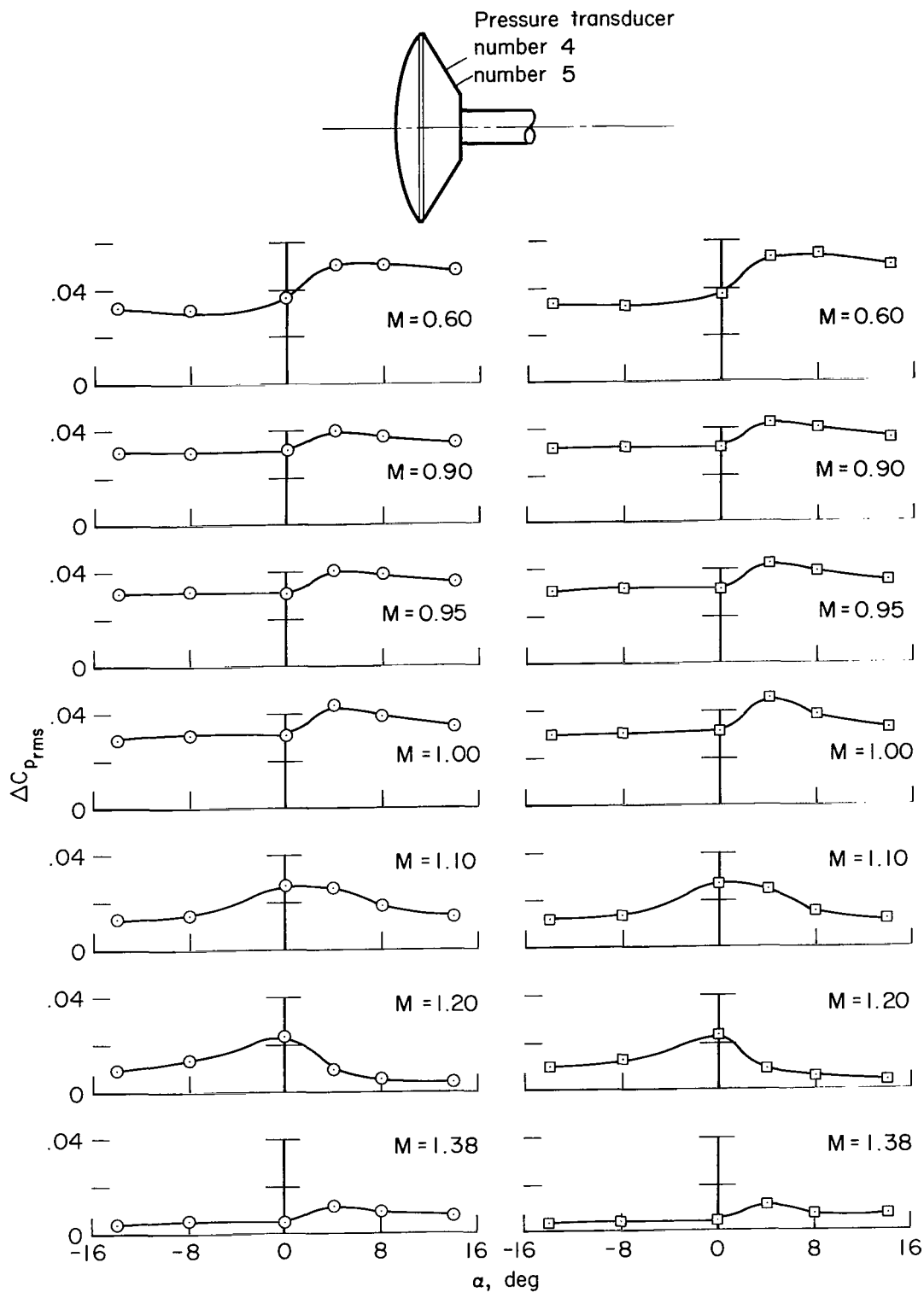
(b) Pressure transducer number 2.

Figure 13.- Continued.



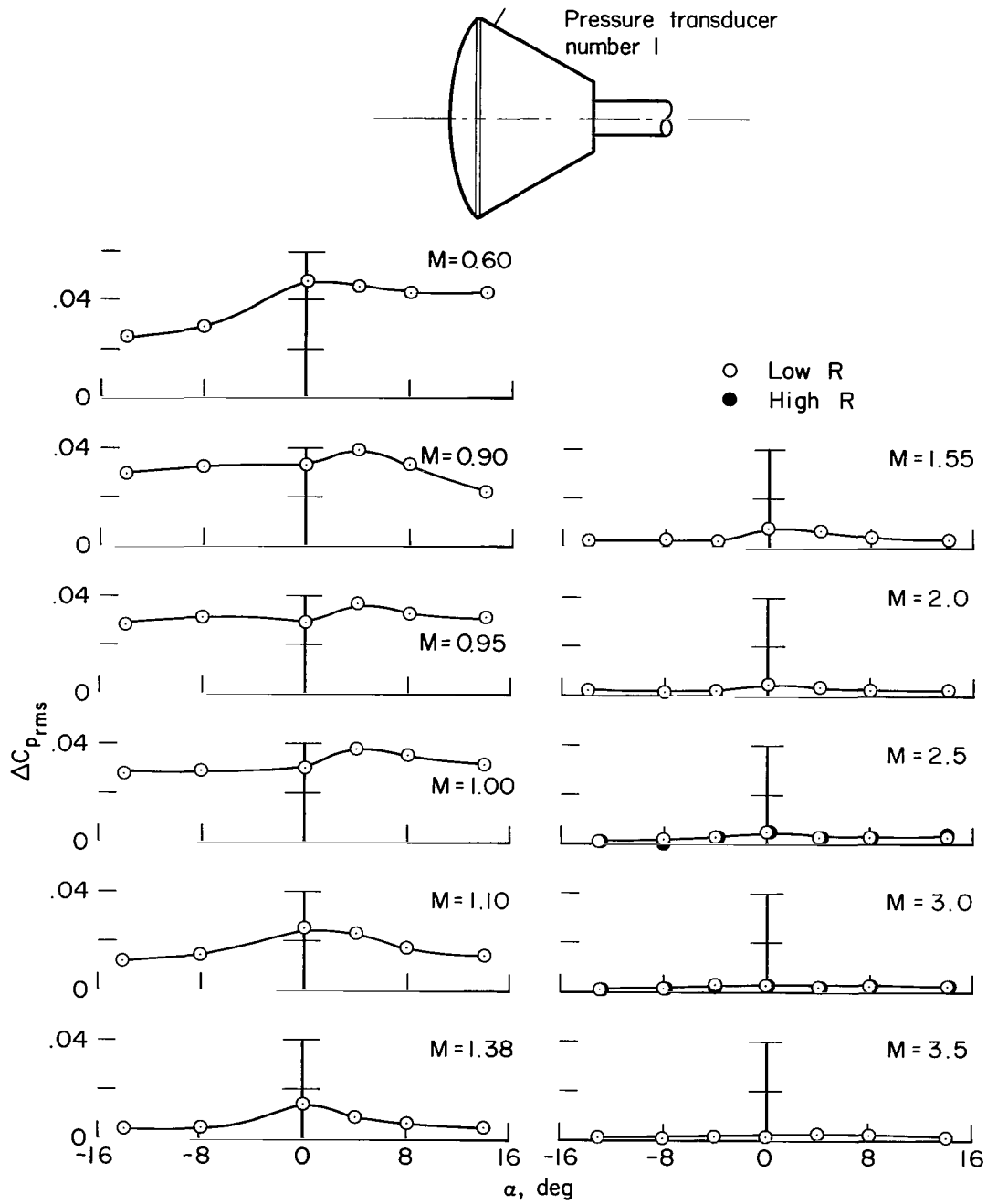
(c) Pressure transducer number 3.

Figure 13.- Continued.



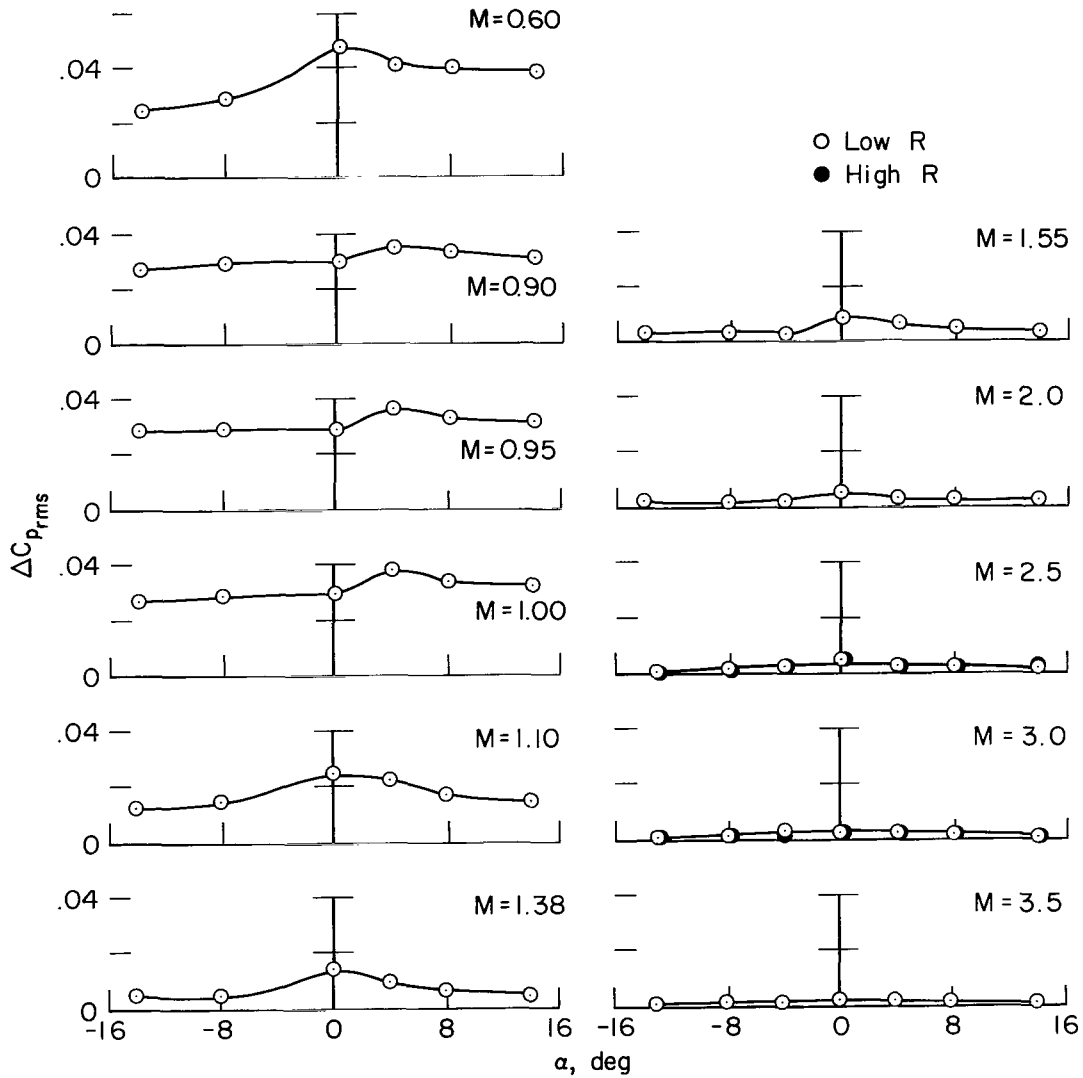
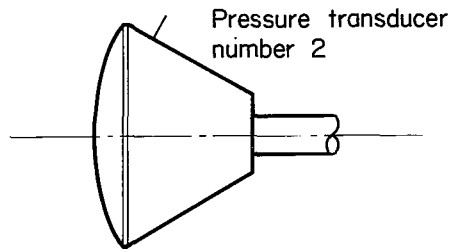
(d) Pressure transducer number 4. (e) Pressure transducer number 5.

Figure 13.- Concluded.



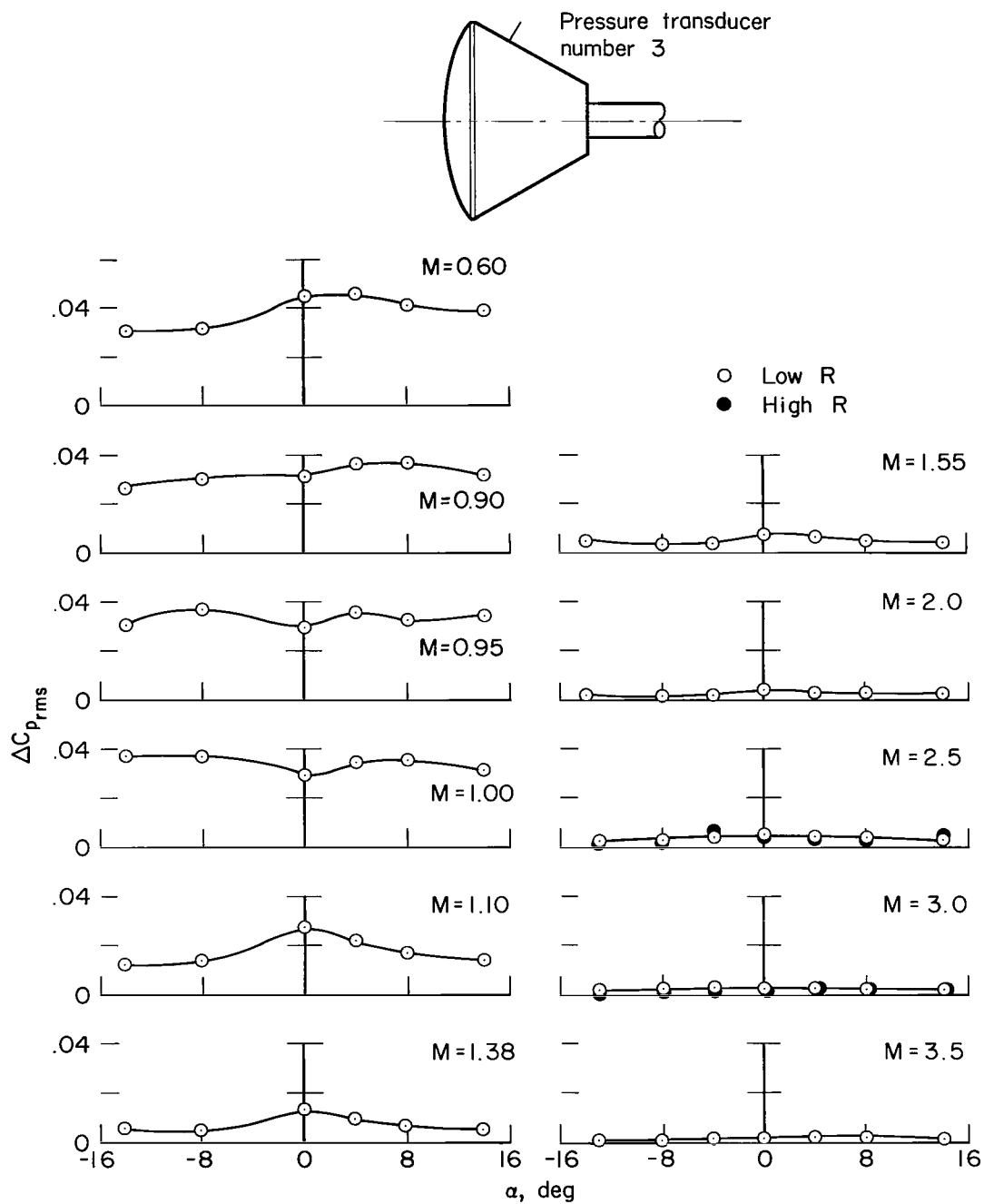
(a) Pressure transducer number 1.

Figure 14.- Pressure fluctuations on model E.



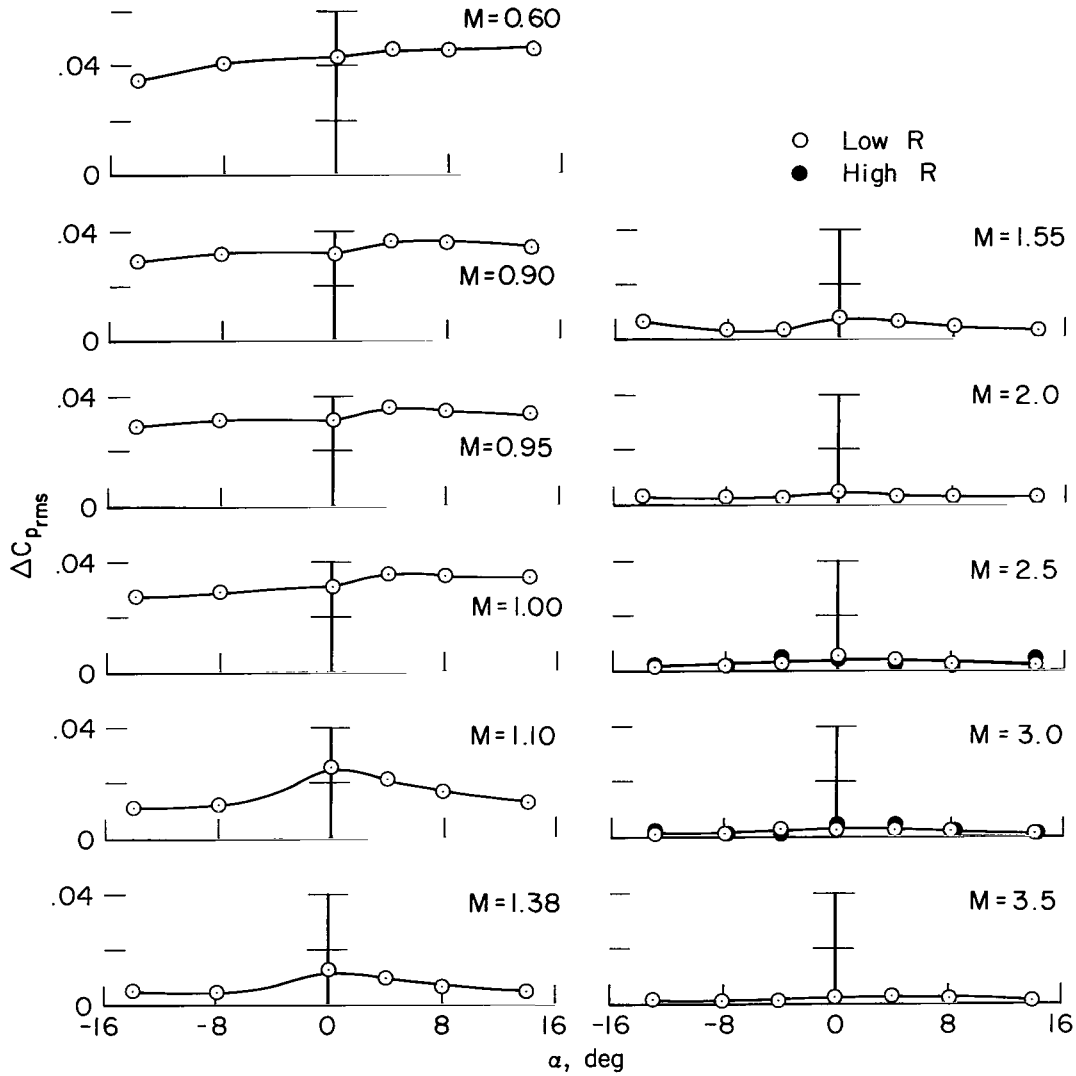
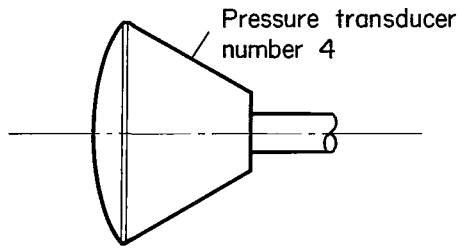
(b) Pressure transducer number 2.

Figure 14.- Continued.



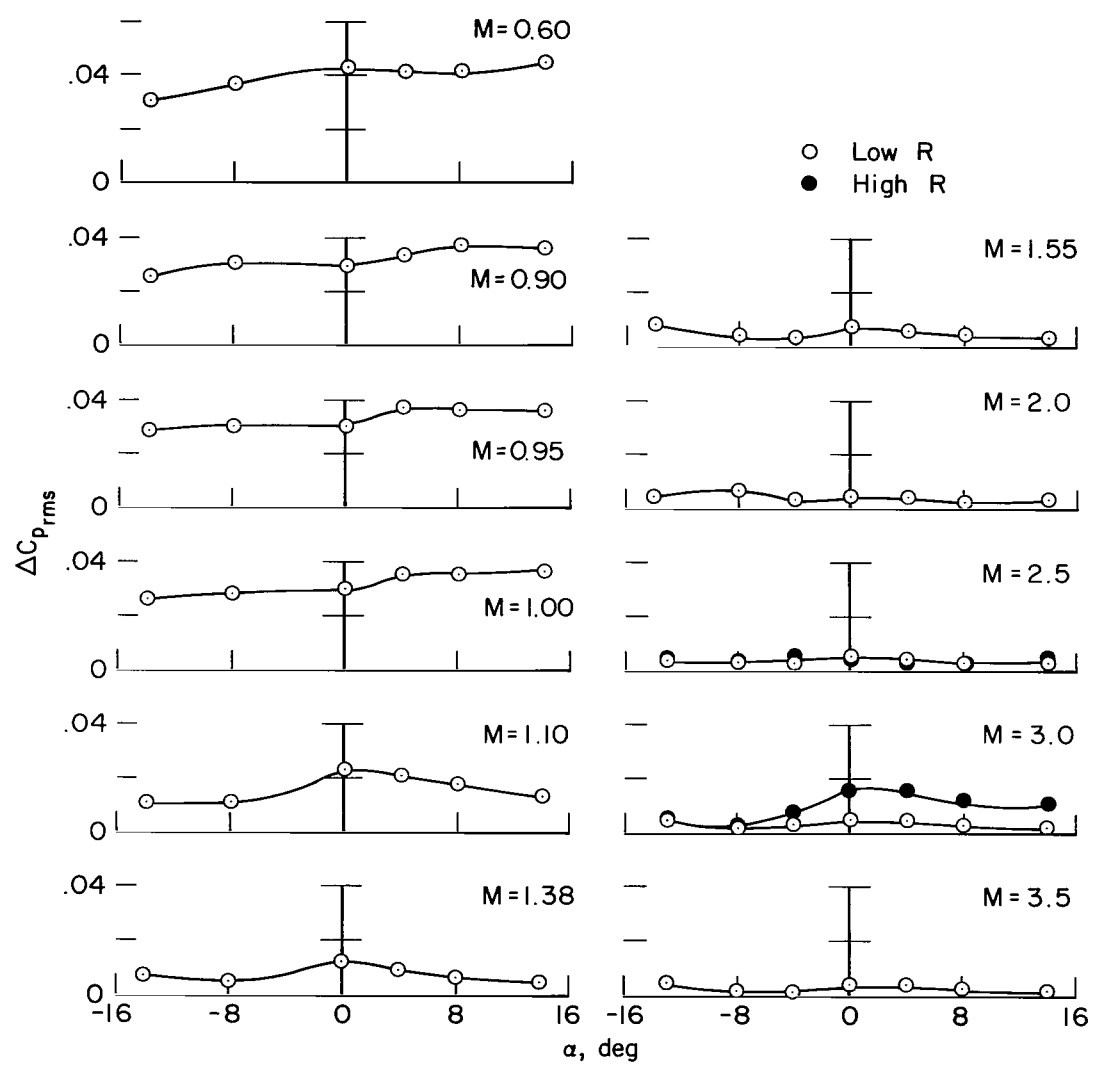
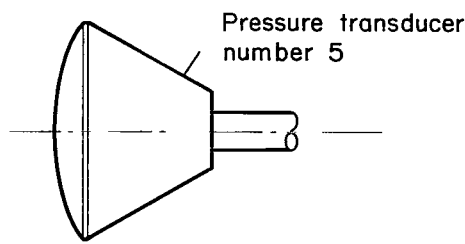
(c) Pressure transducer number 3.

Figure 14.- Continued.



(d) Pressure transducer number 4.

Figure 14.- Continued.



(e) Pressure transducer number 5.

Figure 14.- Concluded.

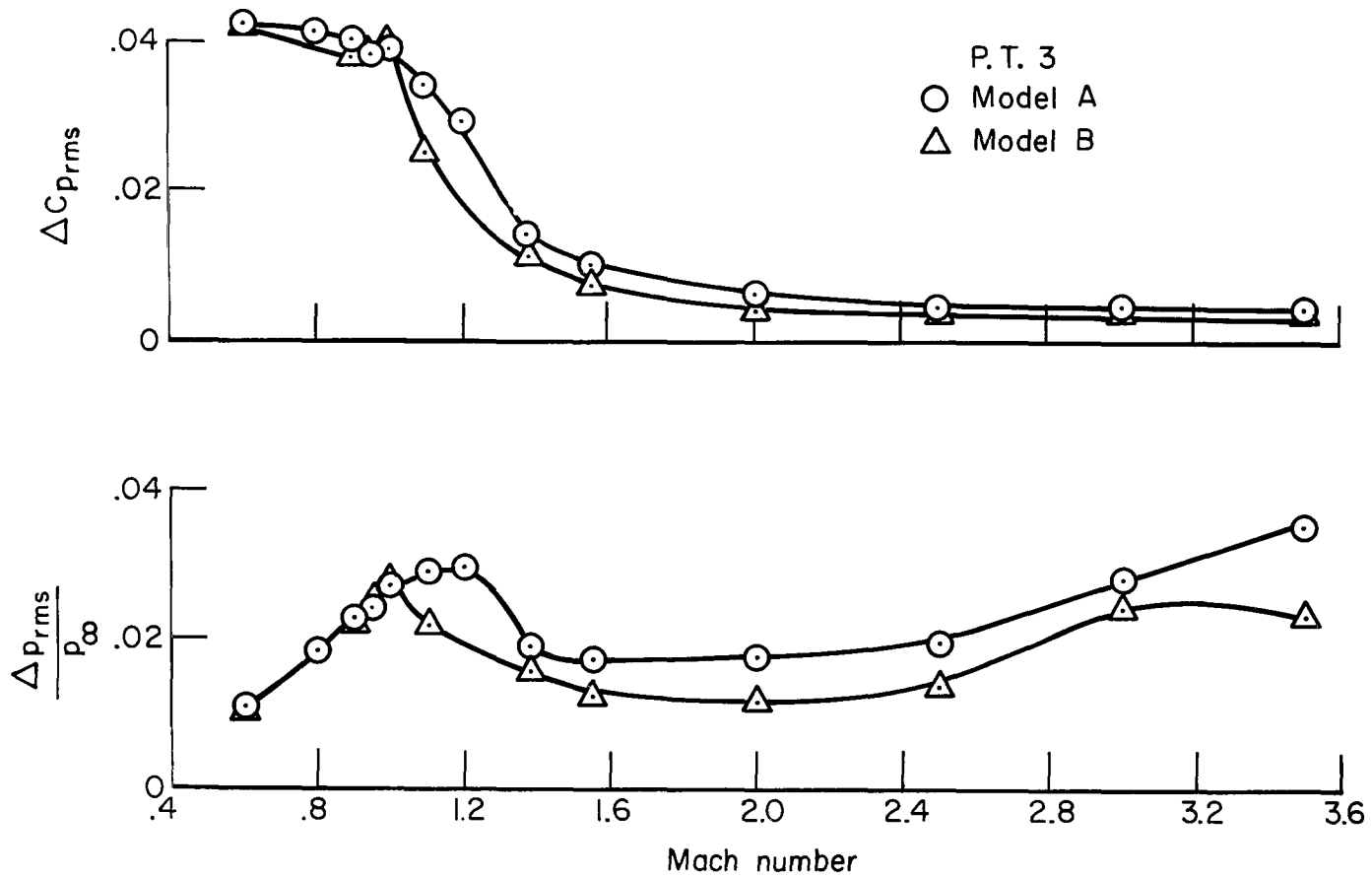
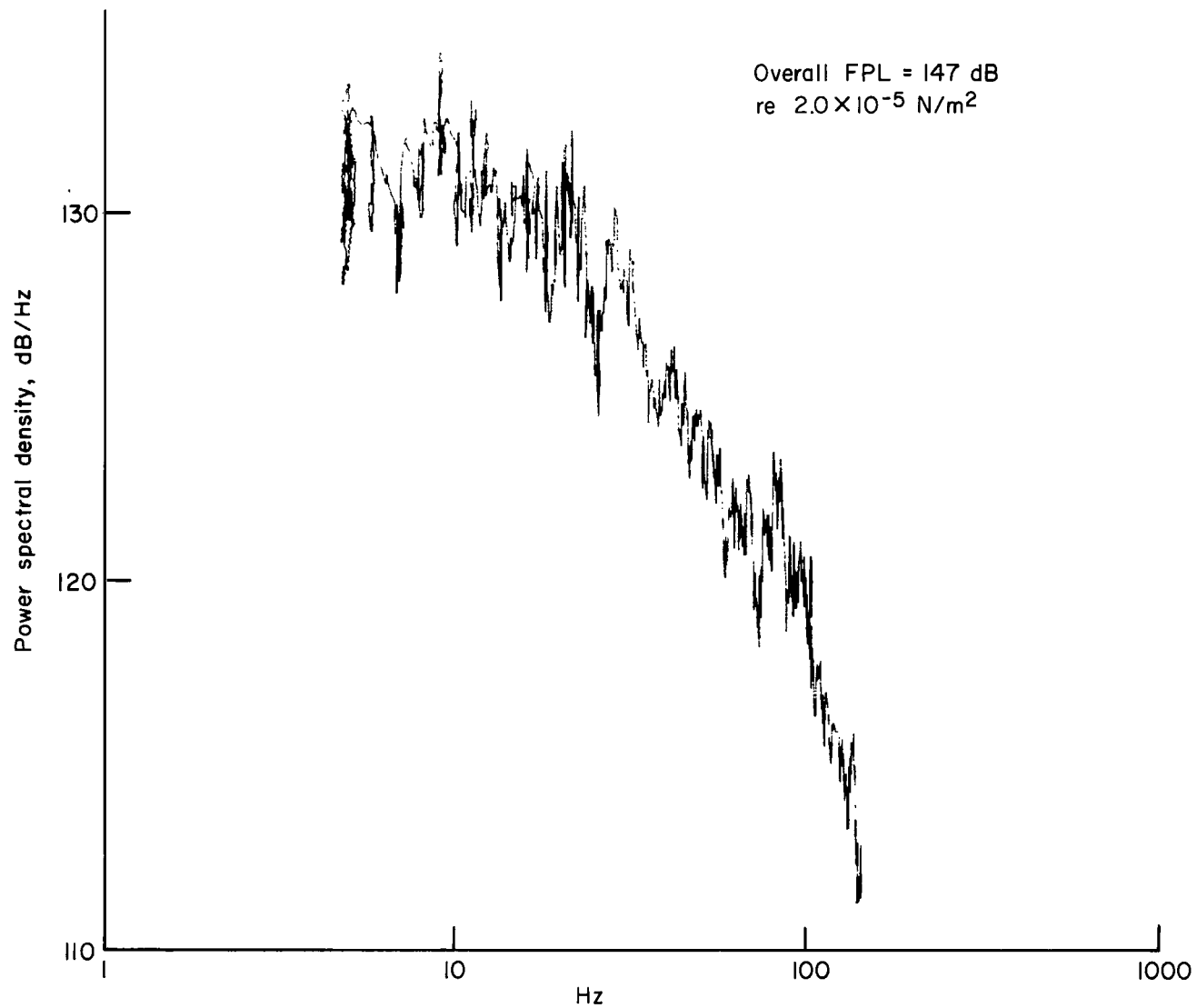
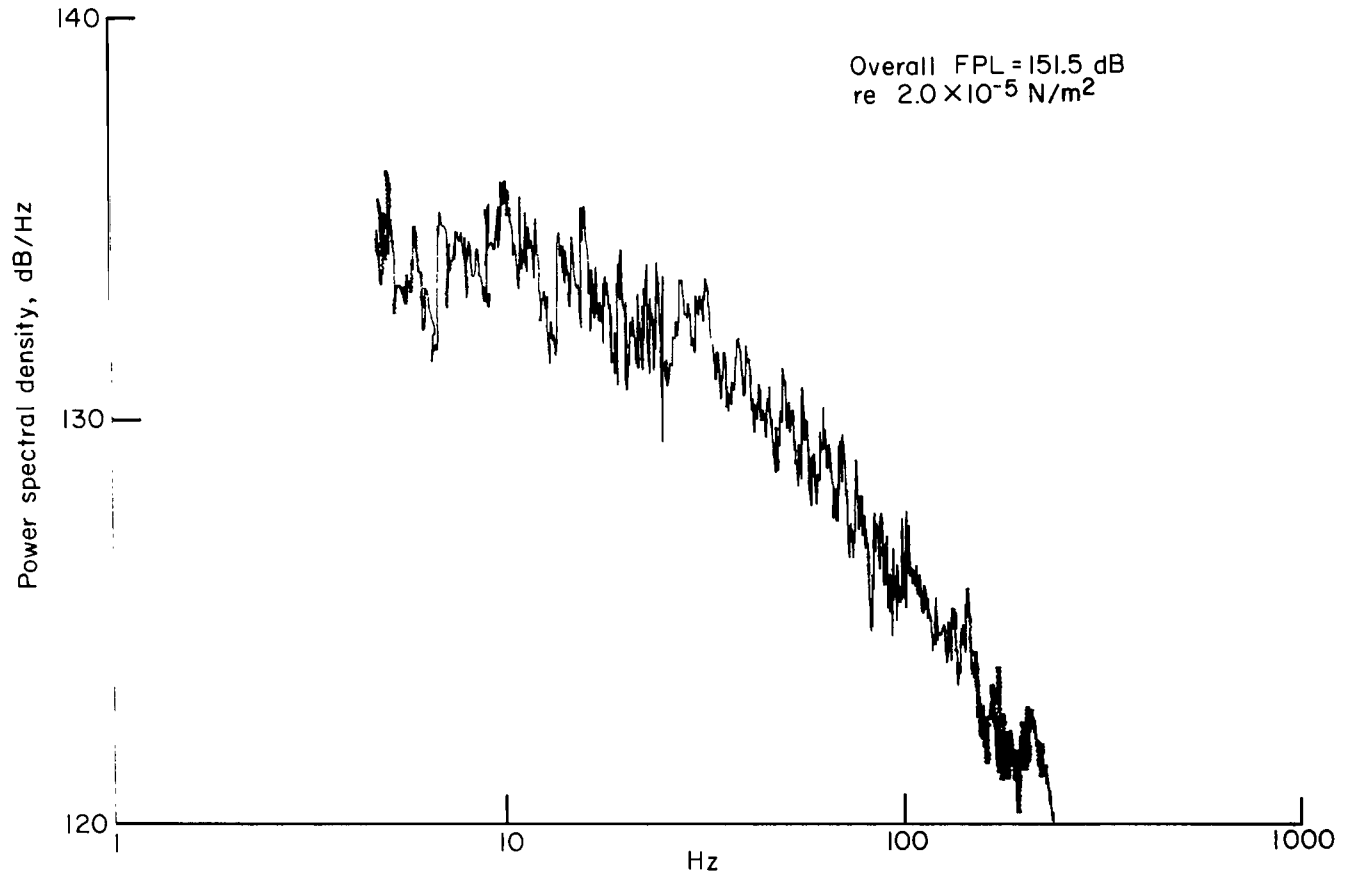


Figure 15.- The effect of Mach number on the pressure fluctuations at  $\alpha = 4^\circ$ .

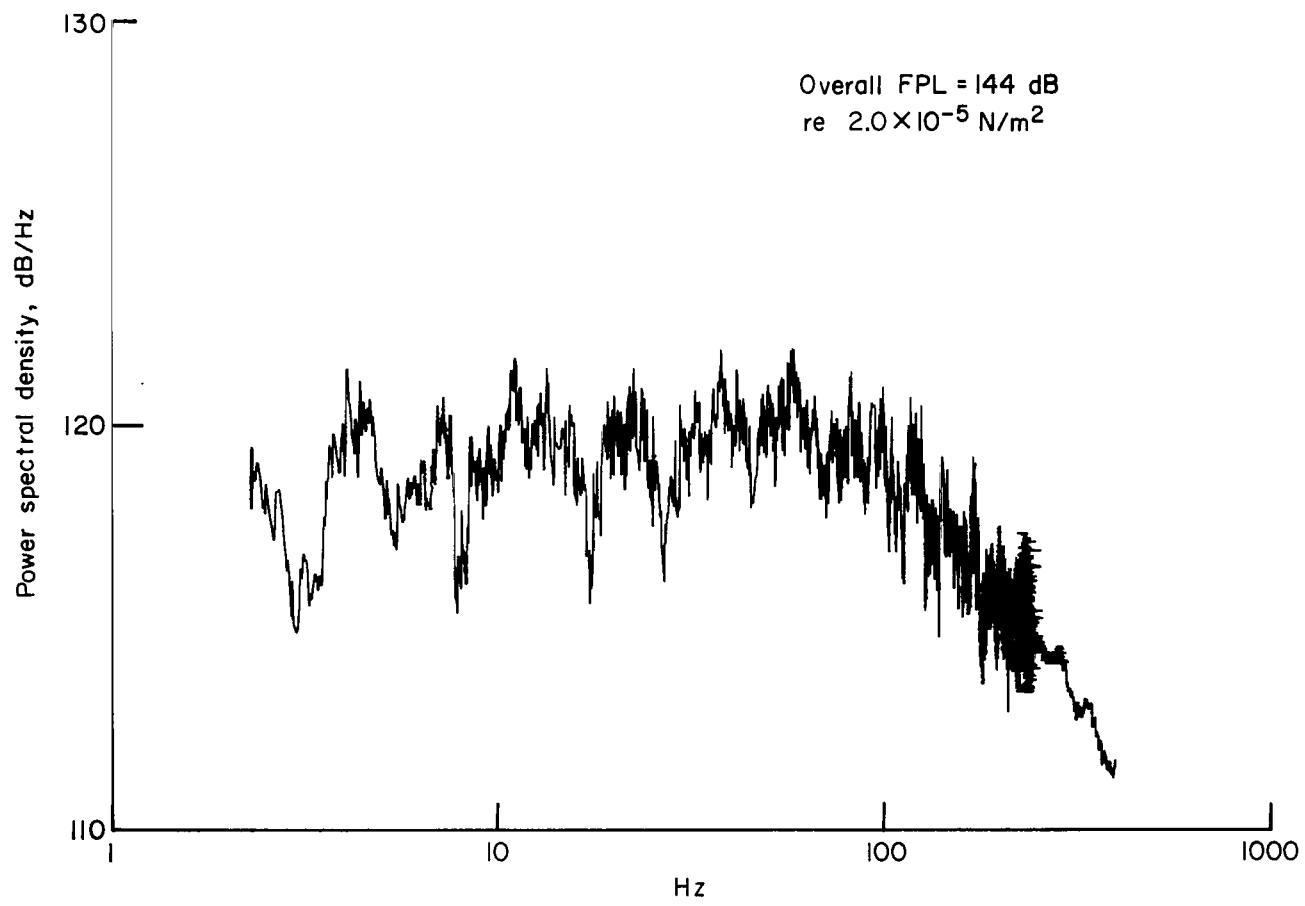


(a)  $M = 0.60$



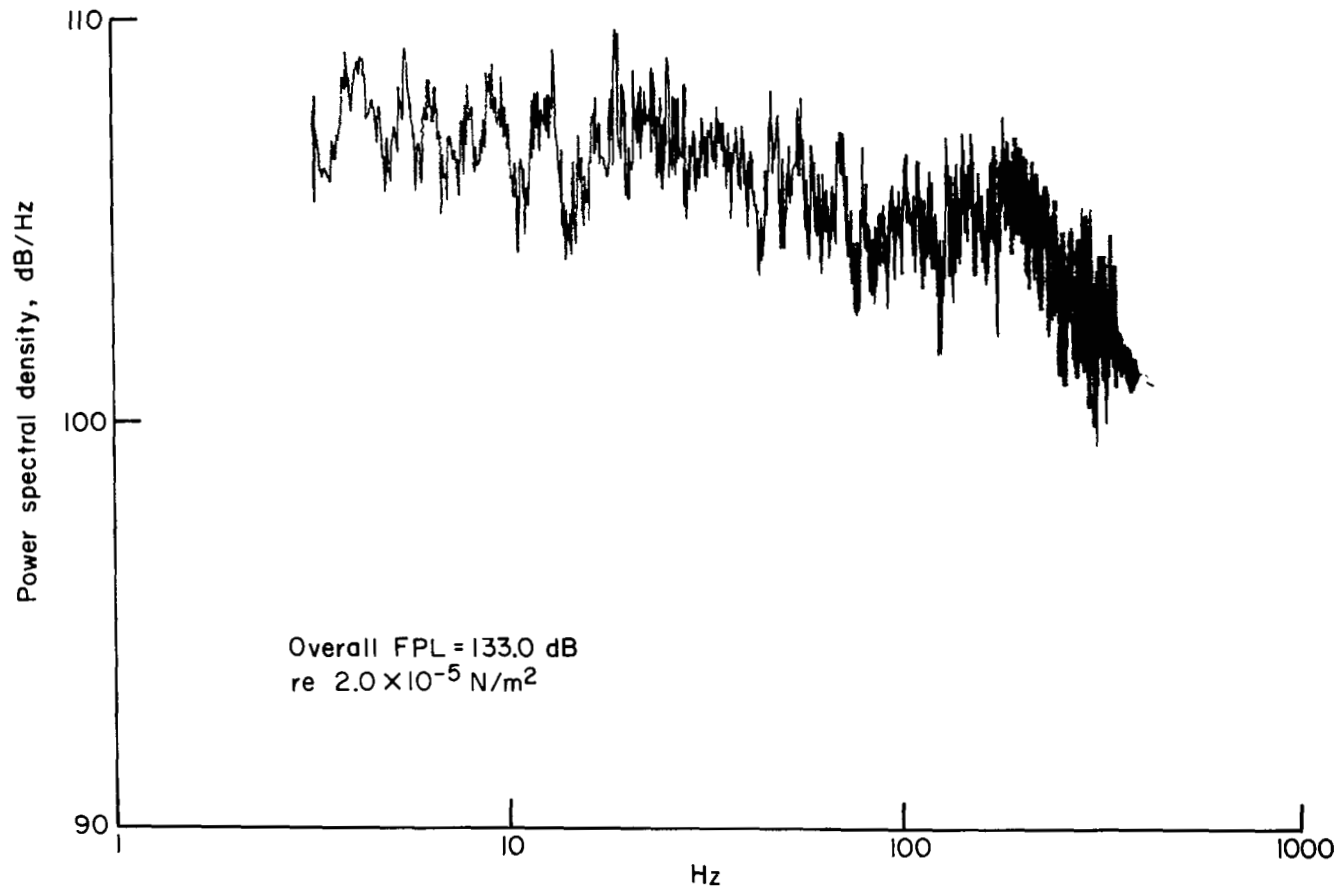
(b)  $M = 1.00$

Figure 16.- Continued.



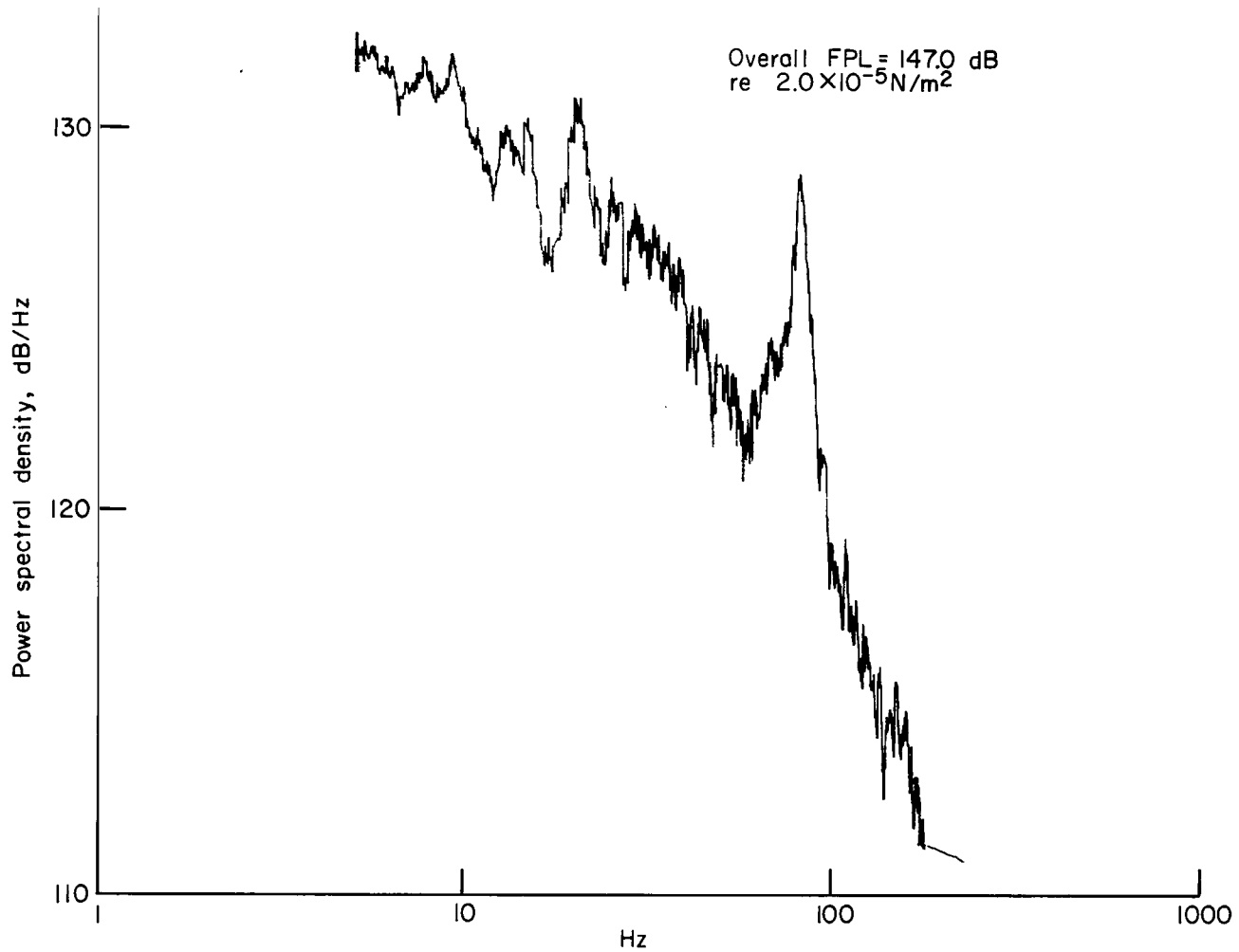
(c)  $M = 1.38$

Figure 16.- Continued.



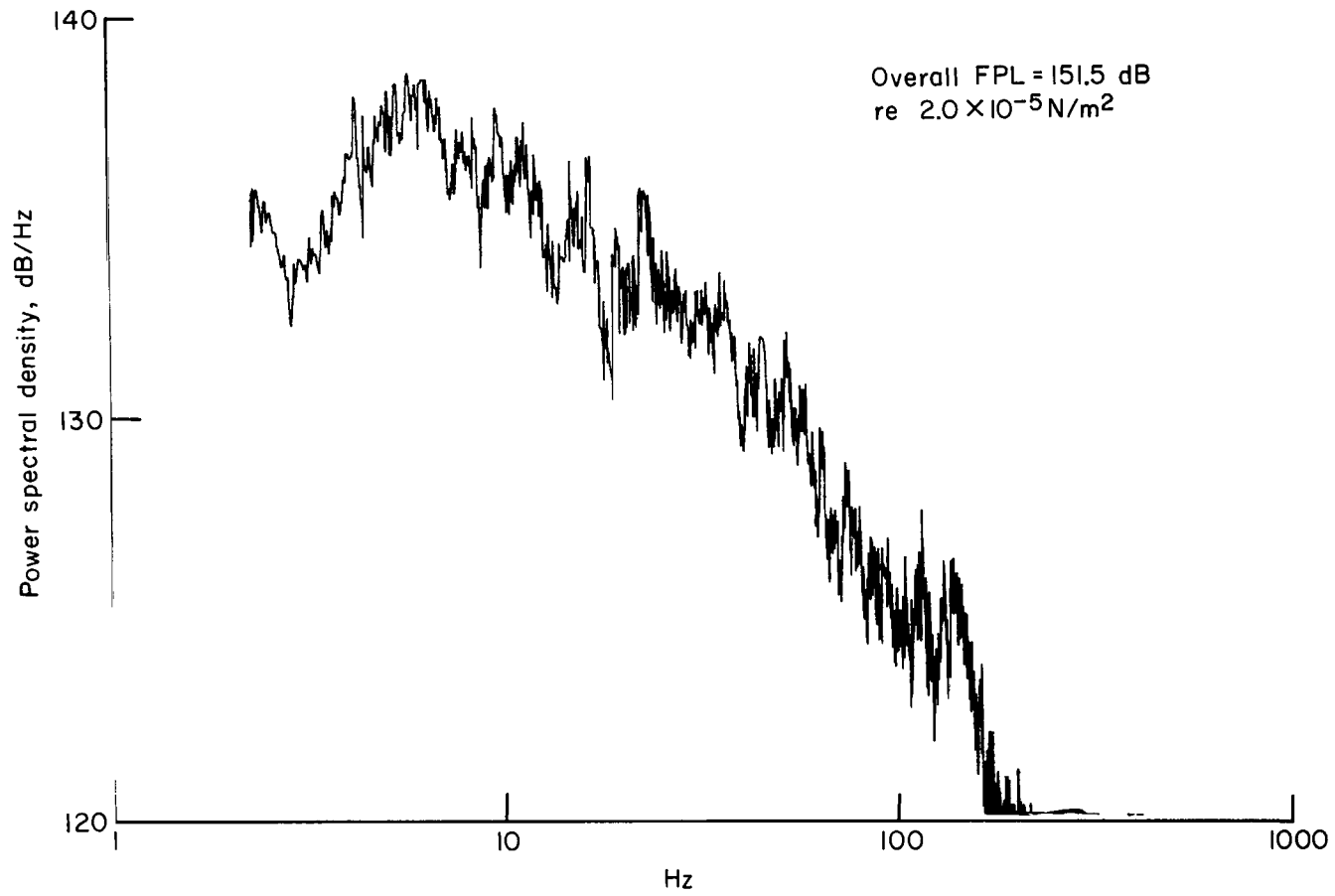
(d) M = 3.00

Figure 16.- Concluded.



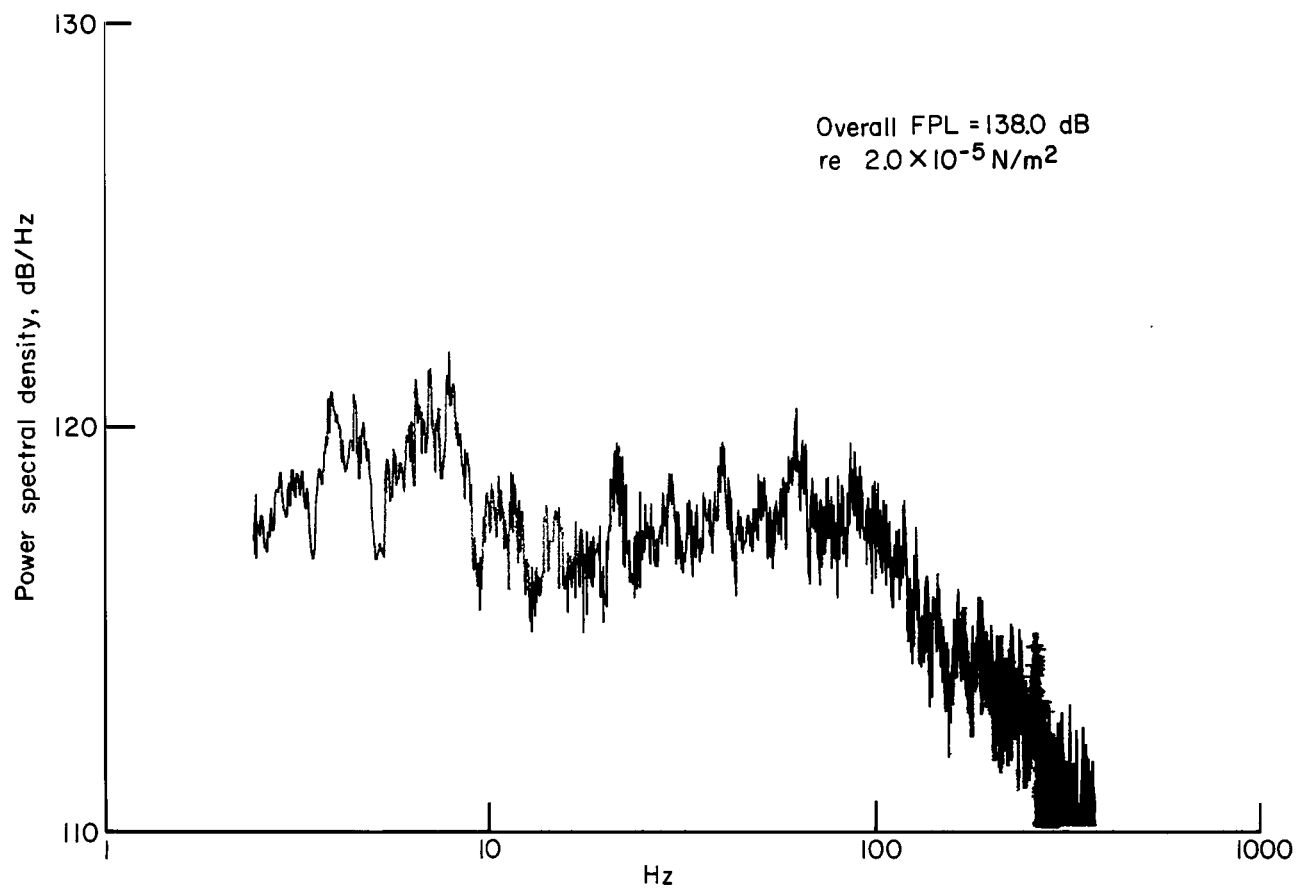
(a)  $M = 0.60$

Figure 17.- Power spectral density of the pressure fluctuations at P.T. 3 on model B for  $\alpha = 4^\circ$ .



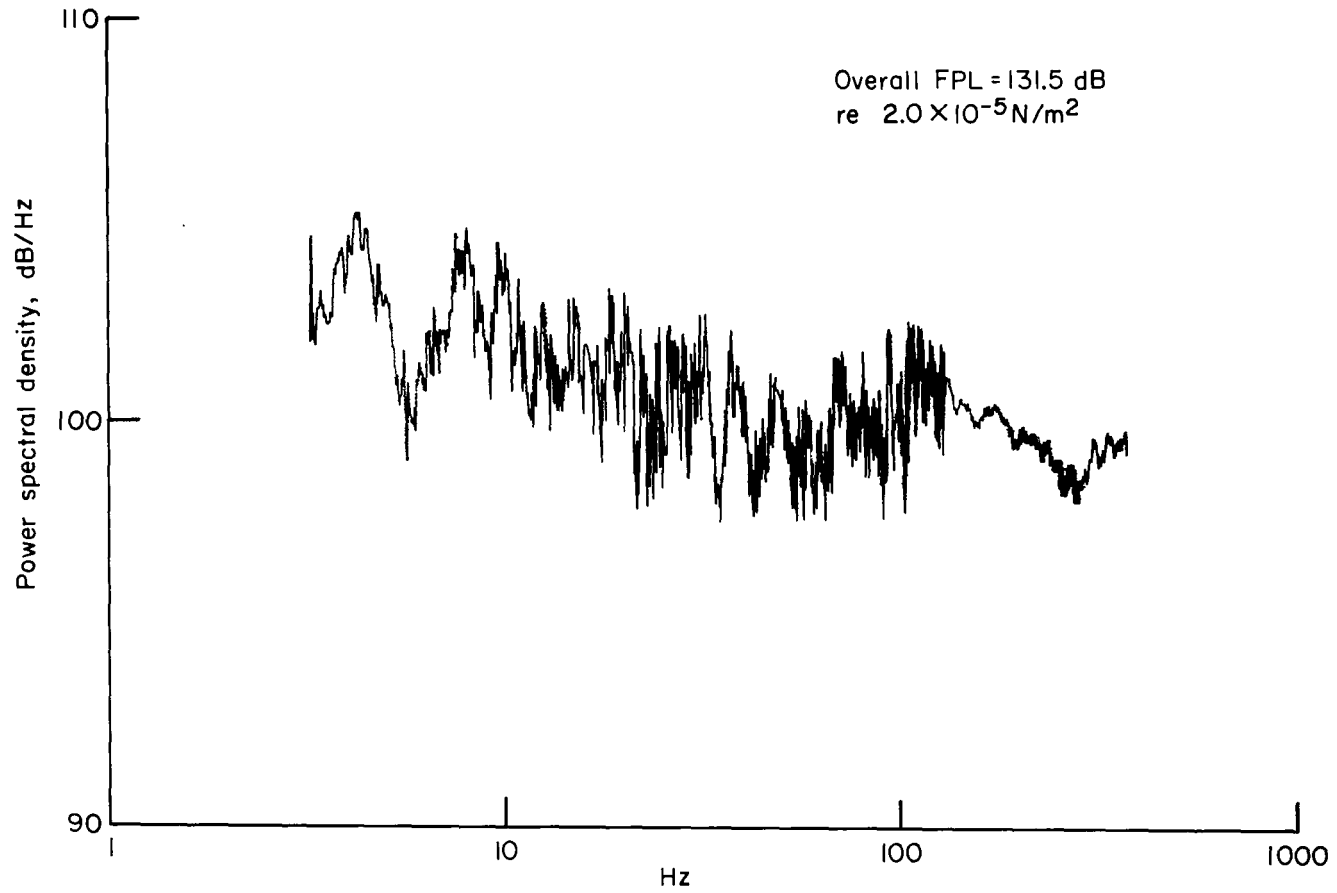
(b)  $M = 1.00$

Figure 17.- Continued.



(c)  $M = 1.38$

Figure 17.- Continued.



(d)  $M = 3.00$

Figure 17.- Concluded.

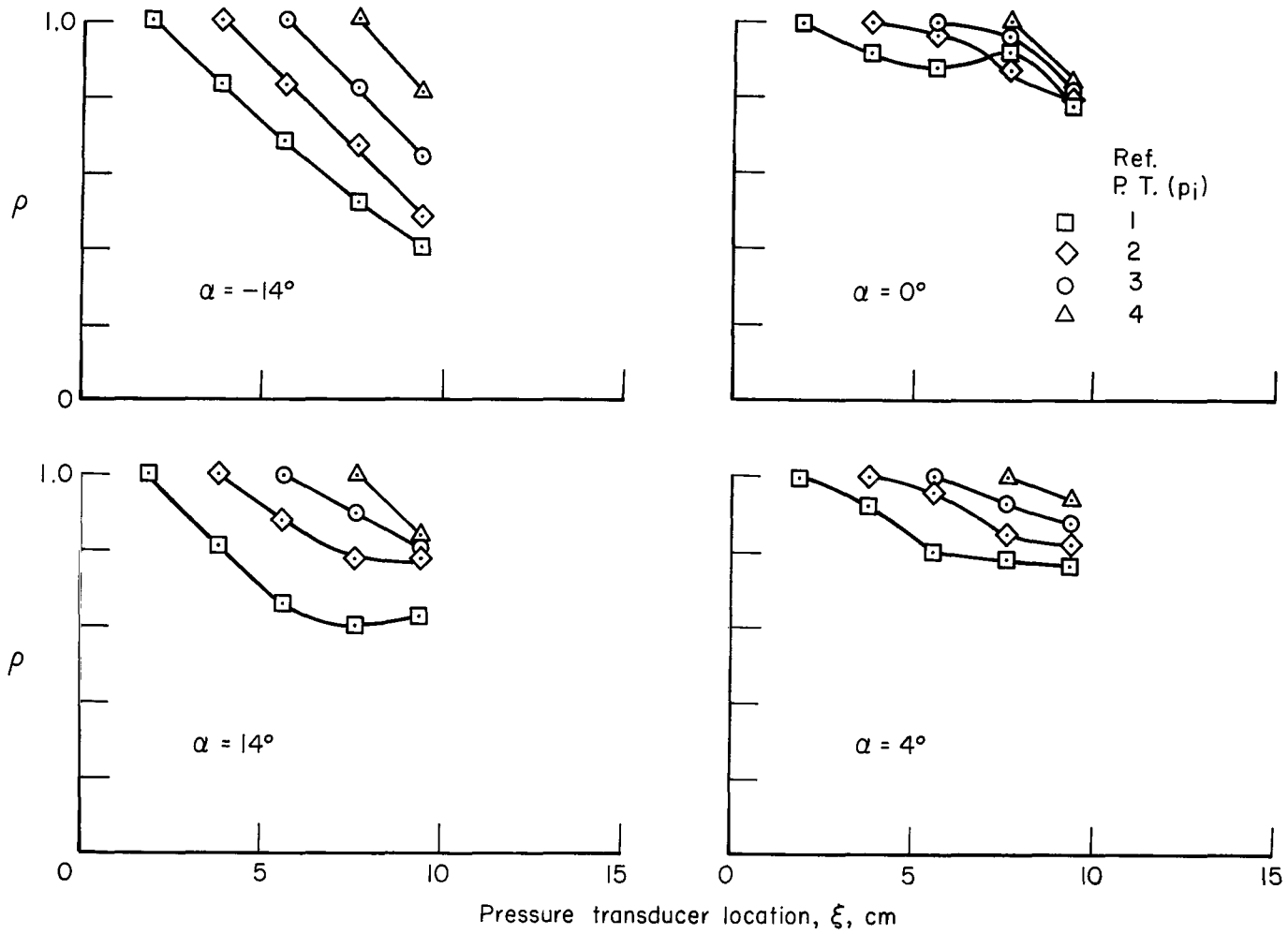


Figure 18.- Correlation of the pressure fluctuations along the afterbody of model A at  $M = 0.6$  for four angles of attack.

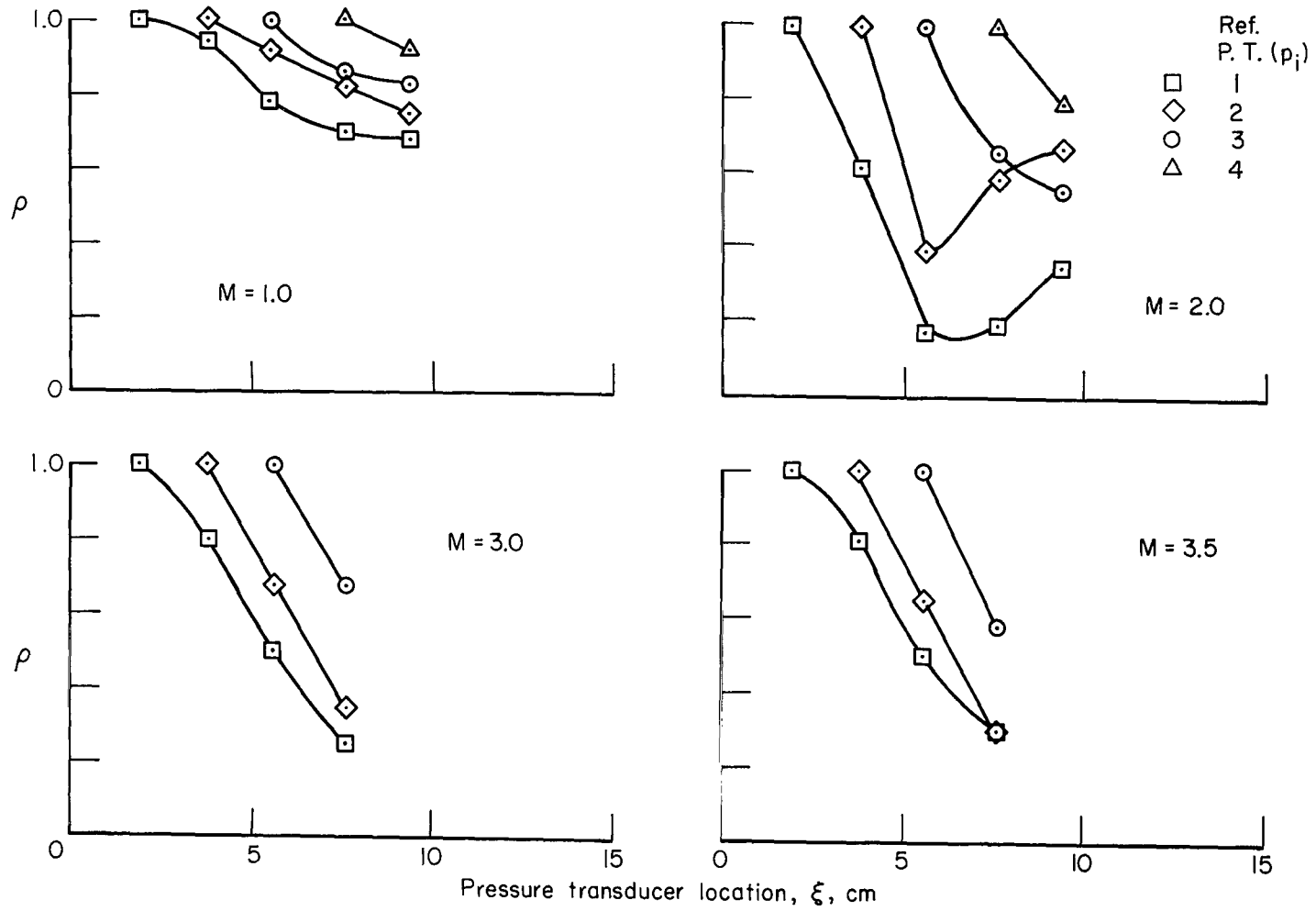


Figure 19.- Correlation of the pressure fluctuations along the afterbody of model A for  $\alpha = 4^\circ$  at four Mach numbers.

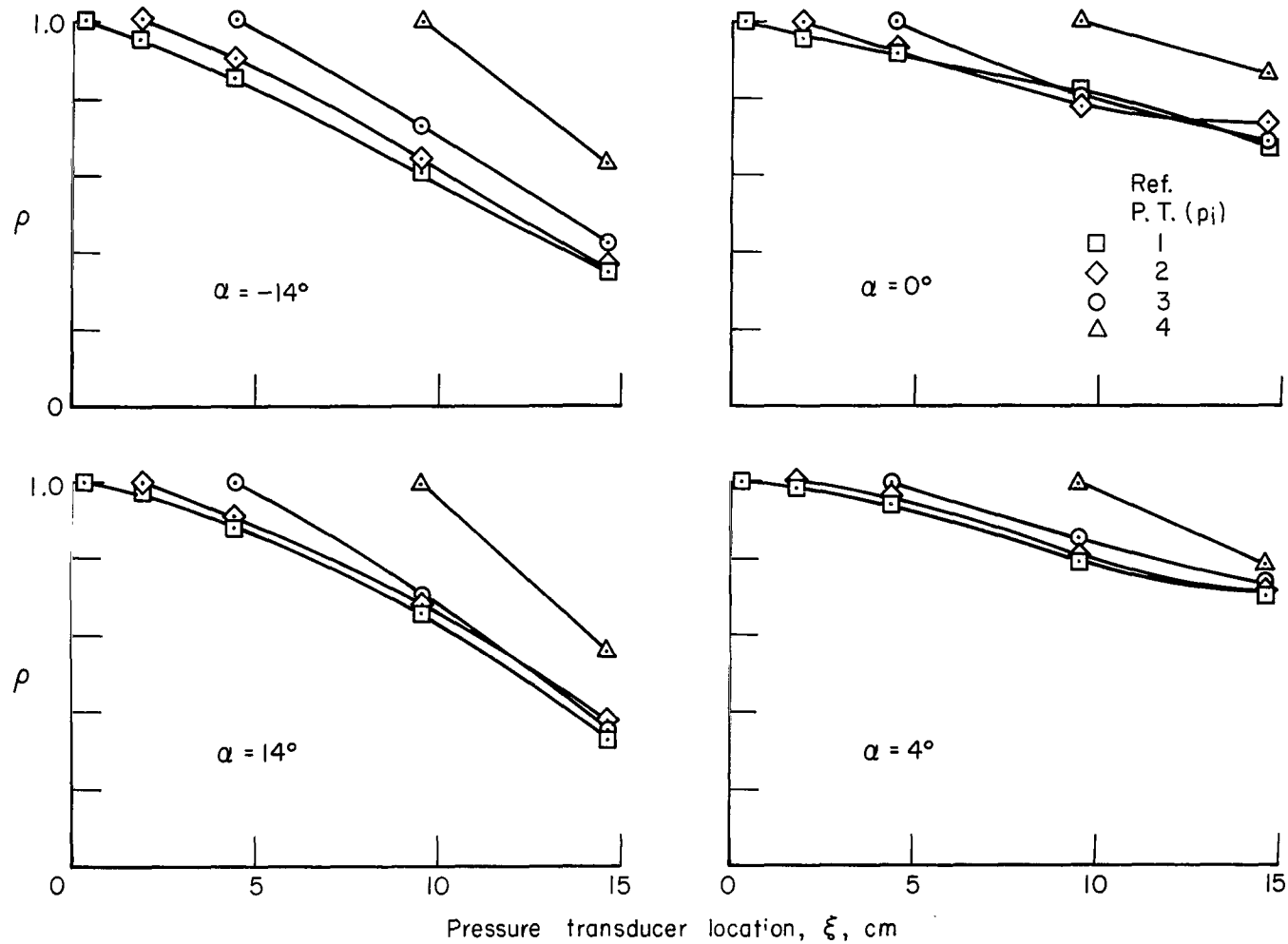


Figure 20.- Correlation of the pressure fluctuations along the afterbody of model B at  $M = 0.6$  for four angles of attack.

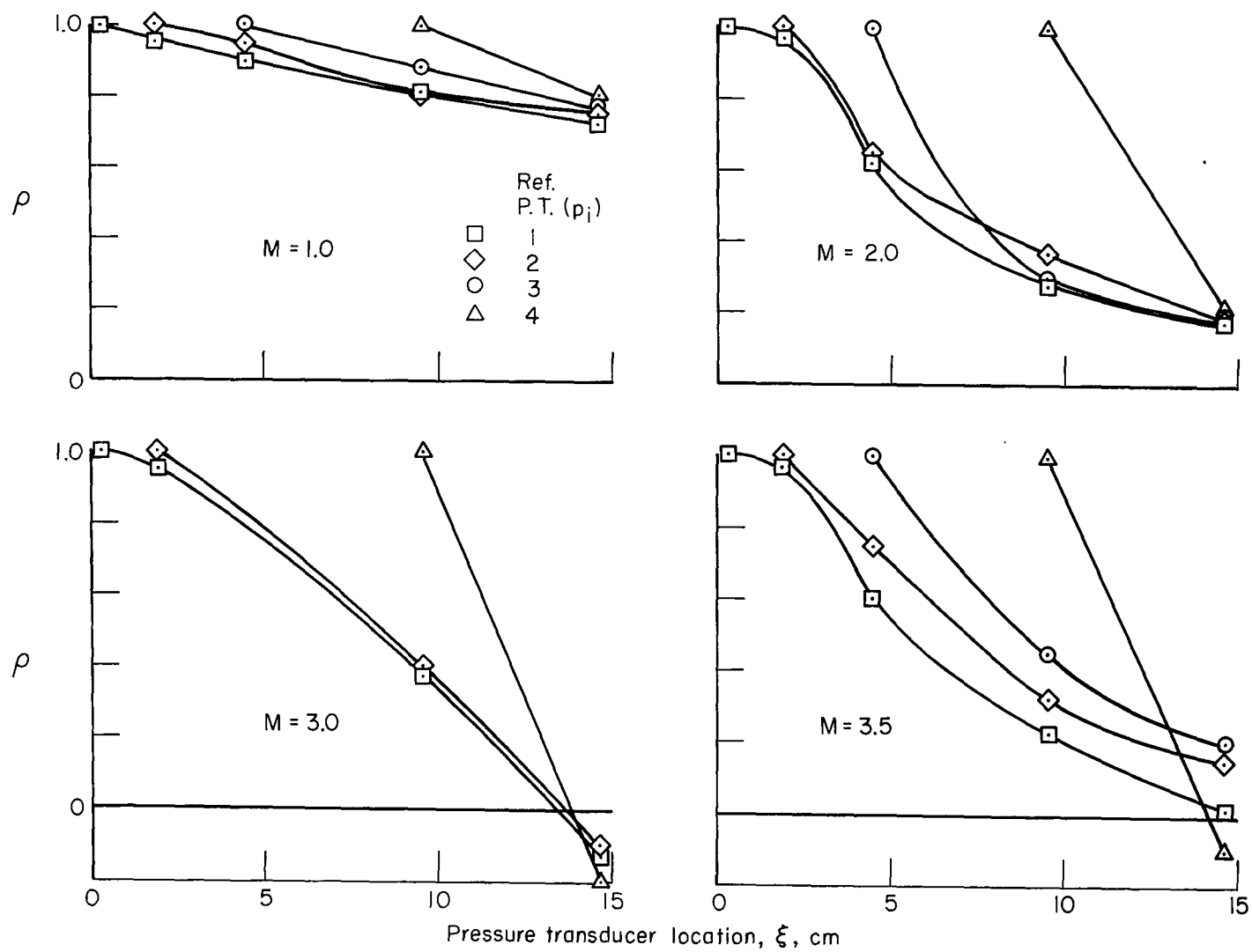
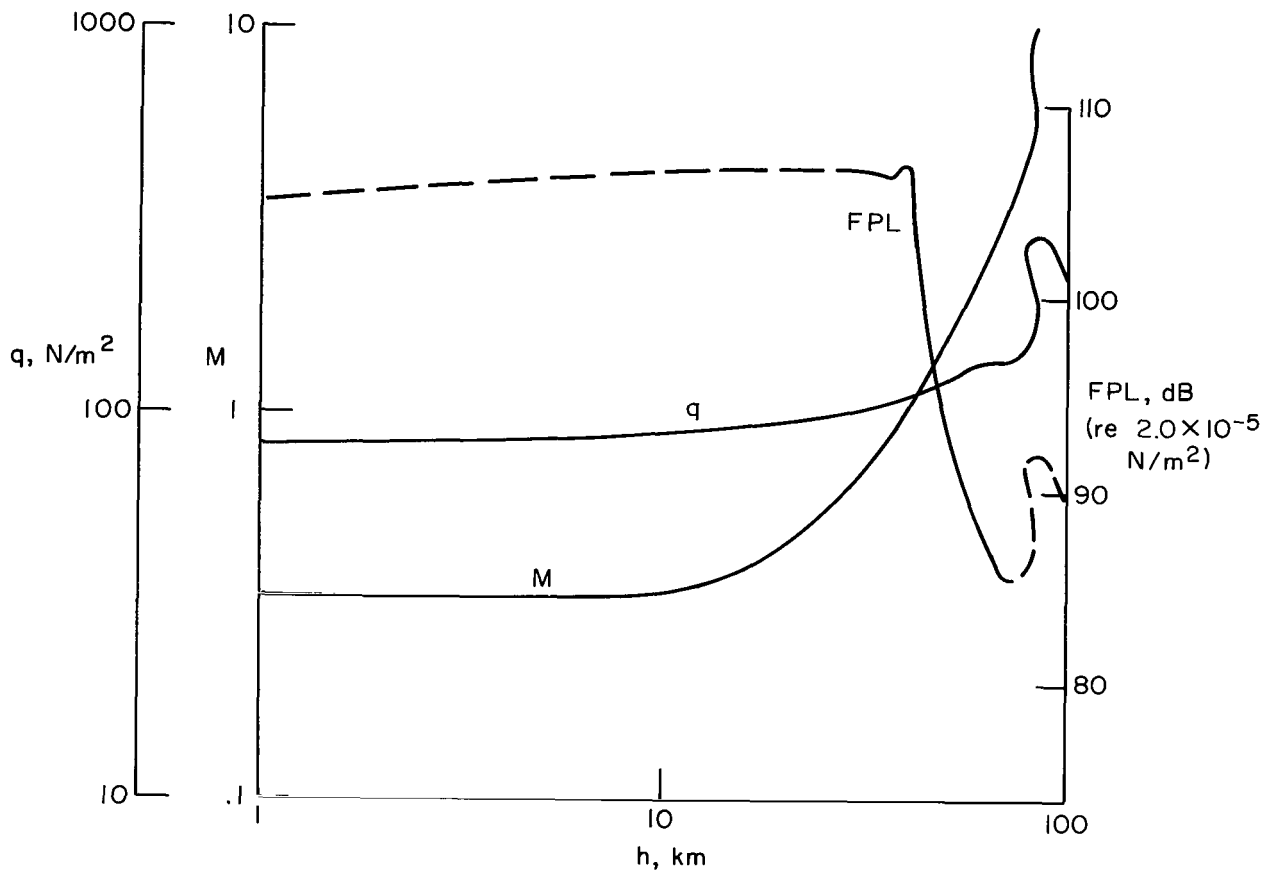
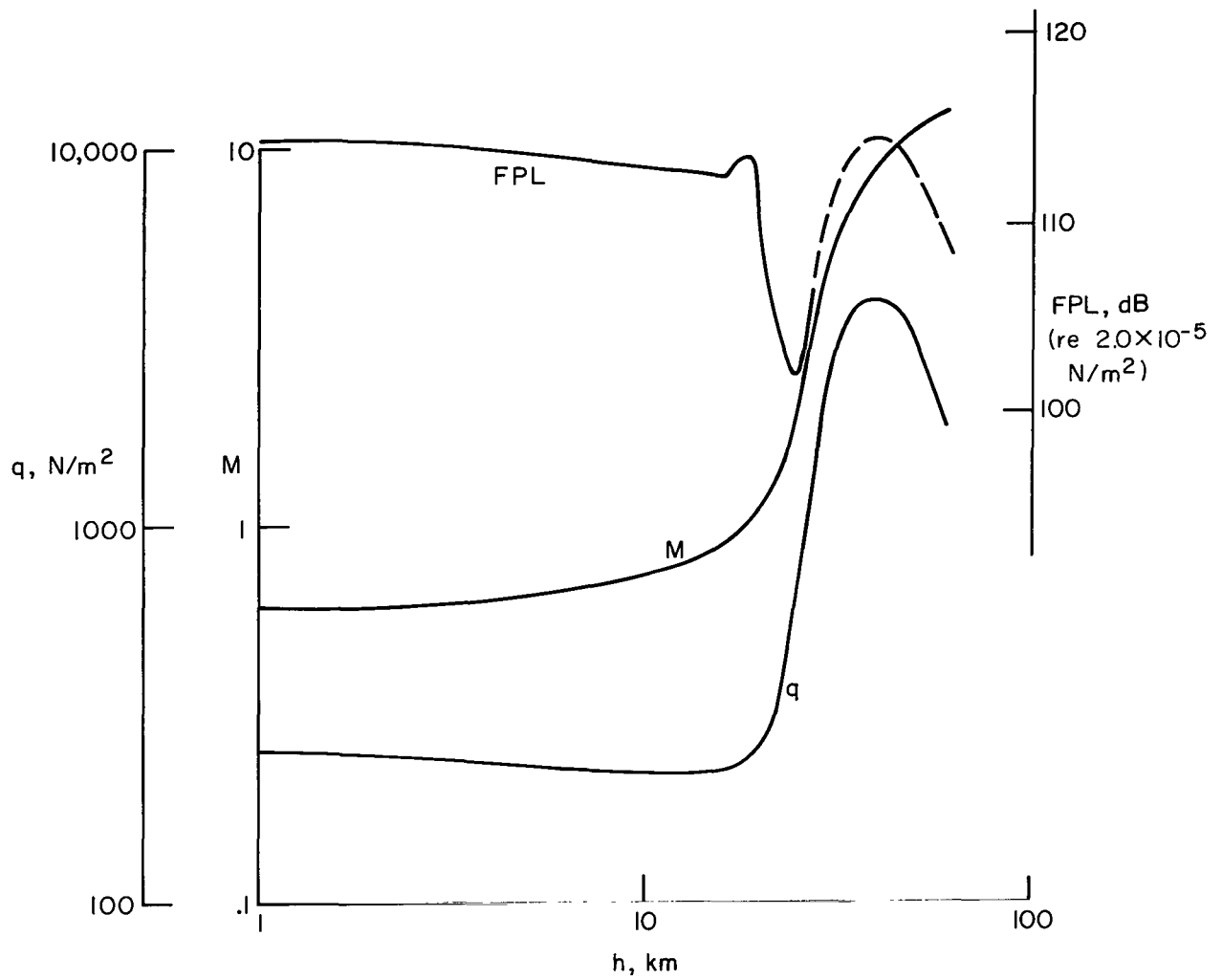


Figure 21.- Correlation of the pressure fluctuations along the afterbody of model B at  $\alpha = 4^\circ$  for four Mach numbers.



(a)  $M/C_{DA} = 23.6 \text{ kg/m}^2$ ,  $\gamma_i = -8^\circ$

Figure 22.- Predicted fluctuating pressure level on the afterbody of model B for entry into the VM3 Mars atmosphere at  $\alpha = 4^\circ$  and an assumed  $L/D$  of 0.25.



(b)  $M/C_D A = 62.8 \text{ kg/m}^2$ ,  $\gamma_i = -24^\circ$

Figure 22.- Concluded.

070 001 26 51 3DS 68134 00903  
AIR FORCE WEAPONS LABORATORY/AFWL/  
KIPTLAND AIR FORCE BASE, NEW MEXICO 8711

ATTN: MISS MAURINE F. CANOVA, CHIEF TECHNICAL  
LIBRARY UNIT

POSTMASTER: If Undeliverable (Section 158  
Postal Manual) Do Not Return

*"The aeronautical and space activities of the United States shall be conducted so as to contribute . . . to the expansion of human knowledge of phenomena in the atmosphere and space. The Administration shall provide for the widest practicable and appropriate dissemination of information concerning its activities and the results thereof."*

— NATIONAL AERONAUTICS AND SPACE ACT OF 1958

## NASA SCIENTIFIC AND TECHNICAL PUBLICATIONS

**TECHNICAL REPORTS:** Scientific and technical information considered important, complete, and a lasting contribution to existing knowledge.

**TECHNICAL NOTES:** Information less broad in scope but nevertheless of importance as a contribution to existing knowledge.

**TECHNICAL MEMORANDUMS:** Information receiving limited distribution because of preliminary data, security classification, or other reasons.

**CONTRACTOR REPORTS:** Scientific and technical information generated under a NASA contract or grant and considered an important contribution to existing knowledge.

**TECHNICAL TRANSLATIONS:** Information published in a foreign language considered to merit NASA distribution in English.

**SPECIAL PUBLICATIONS:** Information derived from or of value to NASA activities. Publications include conference proceedings, monographs, data compilations, handbooks, sourcebooks, and special bibliographies.

**TECHNOLOGY UTILIZATION PUBLICATIONS:** Information on technology used by NASA that may be of particular interest in commercial and other non-aerospace applications. Publications include Tech Briefs, Technology Utilization Reports and Notes, and Technology Surveys.

*Details on the availability of these publications may be obtained from:*

SCIENTIFIC AND TECHNICAL INFORMATION DIVISION  
NATIONAL AERONAUTICS AND SPACE ADMINISTRATION  
Washington, D.C. 20546